

# Improving PM<sub>2.5</sub> forecast over China by the joint adjustment of initial conditions and source emissions with an ensemble Kalman filter

Zhen Peng<sup>1,2</sup>, Zhiquan Liu<sup>2</sup>, Dan Chen<sup>2</sup>, Junmei Ban<sup>2</sup>

<sup>1</sup> School of Atmospheric Sciences, Nanjing University, Nanjing, China

<sup>2</sup> National Center for Atmospheric Research, Boulder, Colorado, USA

**Abstract.** In an attempt to improve the forecasting of atmospheric aerosols, the ensemble square root filter algorithm was extended to simultaneously optimize the chemical initial conditions and emission input. The forecast model, which was expanded by combining the Weather Research and Forecasting with Chemistry (WRF-Chem) model and a forecast model of emission scaling factors, generated both chemical concentration fields and emission scaling factors. The forecast model of emission scaling factors was developed by using the ensemble concentration ratios of the WRF-Chem forecast chemical concentrations and also the time smoothing operator. Hourly surface fine particulate matter (PM<sub>2.5</sub>) observations were assimilated in this system over China from 5 to 16 October 2014. A series of 48-h forecasts were then carried out with the optimized initial conditions and emissions on each day at 0000 UTC and a control experiment was performed without data assimilation. Besides, we also performed an experiment of pure assimilation chemical ICs and the corresponding 48-h forecasts experiment for comparison. The results showed that the forecasts with the optimized initial conditions and emissions typically outperformed those from the control experiment. In the Yangtze River delta and the Pearl River

delta regions, large reduction of the Root Mean Square Errors (RMSEs) was obtained for almost the entire 48-h forecast range attributed to assimilation. Especially, the relative reduction in RMSE due to assimilation was about 37.5% at nighttime when WRF-Chem performed comparatively worse. In the Beijing–Tianjin–Hebei region, relatively smaller improvements were achieved in the first 24-h forecast. Comparing to the forecasts with only the optimized ICs, the forecasts with the joint adjustment were always much better for almost all the forecasts in the PRD and YRD, although they were very similar in the JJJ region.

## **1. Introduction**

Aerosol prediction by regional air quality model in heavy polluted regions is challenging due to many factors. In addition to the deficiency of chemistries, the uncertainties of primary and precursor emissions and the initial conditions (ICs) also limit the forecast accuracy. Data assimilation (DA), which is used to improve the ICs of aerosols and to optimize data on aerosol emissions, has been shown to be one of the most effective ways to improve the forecasting of aerosol pollution.

From the perspective of reducing the uncertainties in the ICs for aerosols, recent efforts have focused on assimilating aerosol observations using optimal interpolation (Collins et al., 2001; Yu et al., 2003; Adhikary et al., 2008; Tombette et al., 2009; Lee et al., 2013) or variational (Kahnert, 2008; Zhang et al., 2008; Benedetti et al., 2009; Pagowski et al., 2010; Liu et al., 2011; Schwartz et al., 2012; Li et al., 2013; Jiang et al., 2013; Saide et al., 2013) DA algorithms. Ensemble-based DA algorithms, such as the ensemble Kalman filter (EnKF) (Sekiyama et al., 2010; Schutgens et al., 2010a, 2010b; Pagowski and Grell, 2012; Dai et al., 2014; Rubin et al., 2016; Ying, X.M., et al., 2016; Yumimoto et al., 2016) and the hybrid variational-ensemble DA approach (Schwartz et al., 2014) have also been applied to aerosol predictions. All these studies have shown that DA is one of the most effective ways of improving aerosol

forecasting through assimilating aerosol observations from multiple sources (e.g. ground-based observations and satellite measurements) to update the chemical ICs.

Numerous studies have used DA approaches to estimate or improve source emissions. The EnKF is one of the most popular DA algorithms used to improve estimates of aerosols and gas-phase emissions, such as  $\text{NO}_x$ , volatile organic compounds, and  $\text{SO}_2$  (van Loon et al., 2000; Heemink and Segers, 2002; Zhang et al., 2005; Barbu et al., 2009; Sekiyama et al., 2010; Huneus et al., 2012; Schutgens et al., 2012; Huneus et al., 2012, 2013; Miyazaki et al., 2014). Variational DA algorithms have also been applied to constrain emissions of air pollution, such as black carbon, organic carbon, dust,  $\text{NH}_3$ ,  $\text{SO}_x$  and  $\text{NO}_x$  (Hakami et al., 2005; Elbern et al., 2007; Henze et al., 2007, 2009; Yumimoto et al., 2007, 2008; Dubovik et al., 2008; Wang et al., 2012; Guerrette and Henze, 2015). These studies have indicated that DA can efficiently reduce the uncertainty in the emission inventories and lead to improvements in the forecasting of air quality (Mijling and van der A, 2012).

The optimization of chemical ICs and pollution emissions can improve aerosol forecasts and therefore further improvements are likely to be achieved by simultaneously optimizing the chemical ICs and emissions. Tang et al. (2011) reported that the simultaneous adjustment of the ICs of  $\text{O}_3$ ,  $\text{NO}_x$  and volatile organic compounds and the emissions of  $\text{NO}_x$  and volatile organic compounds produced overall better performance in both the 1-h and 24-h ozone forecasts than the adjustment of pure ICs or emissions. Miyazaki et al. (2012) reported that the simultaneous adjustment of emissions and concentrations is a powerful approach to correcting the tropospheric ozone budget and profile analyses.

We developed a system to adjust the chemical ICs and source emissions jointly within an EnKF system coupled to the Weather Research and Forecasting with Chemistry (WRF-Chem) model (Grell et al., 2005). We then applied this system to assimilate hourly surface  $\text{PM}_{2.5}$  measurements over China in early October 2014.

The remainder of the paper is organized as follows. Section 2 describes this DA system in detail. Then the experimental designs are introduced in Section 3. Finally, the surface  $\text{PM}_{2.5}$  observations assimilation results are presented in section 4 before

concluding in section 5.

## **2. Methodology**

### **2.1 Forecast model**

For a chemical model like WRF-Chem, the emissions are the model forcing (or boundary condition), rather than model states. Therefore, a forecasting model, **M**, was developed to forecast the emission scaling factors (representing emissions) as well as the aerosol concentrations. This model combines the WRF-Chem model and the forecast model of emission scaling factors.

#### **2.1.1 WRF-Chem model**

Version 3.6.1 of the WRF-Chem model (Grell et al., 2005) was used to forecast the aerosol and chemical species. WRF-Chem is an online model with the fully coupled chemical and meteorological components.

Most of the WRF-Chem settings were the same as those reported in Liu et al. (2011): the Goddard Chemistry Aerosol Radiation and Transport (GOCART) aerosol scheme coupled with the Regional Atmospheric Chemistry Mechanism for gaseous chemical mechanisms; the WRF single-moment five-class microphysics scheme; the Rapid Radiative Transfer Model longwave and Goddard shortwave radiation schemes; the Yonsei University (YSU) boundary layer scheme; the Noah land surface model; and the Grell-3D cumulus parameterization. For the GOCART aerosol scheme, the aerosol species include 14 defined aerosol species and a 15<sup>th</sup> variable representing unseparated aerosol contributions ( $P_{25}$ ). The 14 defined aerosol species are sulfate, hydrophobic and hydrophilic organic carbon ( $OC_1$  and  $OC_2$ , respectively), hydrophobic and hydrophilic black carbon ( $BC_1$  and  $BC_2$ , respectively), dust in five particle size bins (effective radii of 0.5, 1.4, 2.4, 4.5 and 8.0  $\mu\text{m}$ ; referred to as  $D_1$ ,  $D_2$ ,  $D_3$ ,  $D_4$  and  $D_5$ , respectively) and sea salt in four particle size bins (effective radii of 0.3, 1.0, 3.25 and 7.5  $\mu\text{m}$  for dry air; referred to as  $S_1$ ,  $S_2$ ,  $S_3$  and  $S_4$ , respectively).

Figure 1 illustrates the model computational domain. It has 120\*120 horizontal

grid scales at a 40.5 km spacing by the lambert conform map projection centered at (35 °N, 105 °E). There are 57 vertical levels with the model top at 10 hPa, about 12 layers within the planetary boundary layer (among them the lowest 8 layers were under 500 m), and the first layer centered at ~12 m.

With respect to the emissions, the hourly prior anthropogenic emissions were based on the monthly regional emission inventory in Asia (Zhang et al., 2009) for the year 2006 interpolated to the model grid. The power generator emissions were interpolated for the lowest eight vertical levels (Woo et al., 2003; de meij et al., 2006; Wang et al., 2010). Other anthropogenic emissions were assigned totally to the 1<sup>st</sup> level. Emissions are very small above 500 m for all pollutants. In order to keep objective for the prior anthropogenic emissions, no time variation was added. Thus, the hourly prior anthropogenic emissions were constant. The biogenic (Guenther et al., 1995), dust (Ginoux et al., 2001), dimethylsulfide and sea salt emissions (Chin et al., 2000, 2002) were calculated online.

### 2.1.2 Forecast model of scaling factors

As no suitable dynamic model was available to forecast the emission scaling factors, a persistence forecasting operator served as the forecast model for the scaling factors, similar to the method used by Peng et al. (2015) for CO<sub>2</sub> emission inversion. Figure 2a shows the flowchart for the persistence forecasting operator  $\mathbf{M}_{\text{SF}}$ .

If the ensemble members of the updated chemical fields  $\mathbf{C}_{i,t-1}^a$  and the forecast emissions  $\mathbf{E}_{i,t-2}^f$  in the previous assimilation cycle are known, then the chemical fields  $\mathbf{C}_{i,t}^f$  at time  $t$  can be generated via WRF-Chem (Figure 2b). In the actual process,  $\mathbf{C}_{i,t}^f$  were available in the previous assimilation cycle, so we did not need to perform the ensemble forecasts again. A dotted box was used in Figure 2a to indicate that the ensemble forecasts were not performed in real process. The ensemble concentration ratios  $\kappa_{i,t}, (i = 1, \dots, N)$  are then calculated using

$$\kappa_{i,t} = \frac{\mathbf{C}_{i,t}^f}{\overline{\mathbf{C}}_t^f}, (i = 1, \dots, N), (1)$$

where  $\overline{\mathbf{C}}_t^f = \frac{1}{N} \sum_{i=1}^N \mathbf{C}_{i,t}^f$  is the ensemble mean of the forecast. The ensemble mean of

140  $\kappa_{i,t}$  is,

141 
$$\overline{\kappa_t} = \frac{1}{N} \sum_{i=1}^N \kappa_{i,t} = \frac{1}{N} \sum_{i=1}^N \mathbf{C}_{i,t}^f / \overline{\mathbf{C}_t^f} = 1, (2)$$

142 so  $\kappa_{i,t}$  are numbers distributed around 1 and with ensemble mean values of 1.

143 The ensemble spreads of  $\kappa_{i,t}, (i = 1, \dots, N)$  may be small and therefore  
144 covariance inflation is used to maintain them at a certain level:

145 
$$(\kappa_{i,t})_{\text{inf}} = \beta(\kappa_{i,t} - \overline{\kappa_t}) + \overline{\kappa_t}, (i = 1, \dots, N), (3)$$

146  $\beta = 1.5$  was chosen to make ensure the ensemble spread of  $(\kappa_{i,t})_{\text{inf}}$  ranged from  
147 0.1 to 1.25 in this study. Same as  $\kappa_{i,t}$ , the ensemble mean values of  $(\kappa_{i,t})_{\text{inf}}$  are 1. It  
148 is noted that perhaps there are very few negative values for  $(\kappa_{i,t})_{\text{inf}}$  after inflation. A  
149 quality control procedure is performed for  $(\kappa_{i,t})_{\text{inf}}$  before further appliance. All  
150 these negative data were set as 0.001 in this work. Then  $(\kappa_{i,t})_{\text{inf}}$  were re-centered to  
151 ensure the ensemble mean values of  $(\kappa_{i,t})_{\text{inf}}$  were all 1.

152 As the concentrations were closely related to the emissions both locally and in  
153 the upwind regions and there is no suitable dynamic model available to forecast the  
154 emission scaling factors, the inflated concentration ratios  $(\kappa_{i,t})_{\text{inf}}$  serve as the prior  
155 emission scaling factors  $\lambda_{i,t}^p$ :

156 
$$\lambda_{i,t}^p = (\kappa_{i,t})_{\text{inf}}, (i = 1, \dots, N), (4)$$

157 The above equation is not supported according to the mass conservation equation  
158 but just for the purpose to generate the ensemble emissions. Same as  $(\kappa_{i,t})_{\text{inf}}$ ,  $\lambda_{i,t}^p$   
159 are numbers distributed around 1. From the perspective of generating the ensemble  
160 emissions, they can play the same role as other data, such as the random numbers  
161 created by using the standard normal distribution function. However, there are  
162 correlations among the grid-points of  $(\kappa_{i,t})_{\text{inf}}$  because  $(\kappa_{i,t})_{\text{inf}}$  are calculated

through a short-term forecast of WRF-Chem. Thus,  $\lambda_{i,t}^p$  have the same correlations as  $(\kappa_{i,t})_{\text{inf}}$ . While, the random numbers are totally different. There are no correlations unless they are generated under certain correlations.

To incorporate the useful information from the previous times, the previous DA cycles' analysis scaling factors,  $\lambda_{i,t-M+1}^a, \dots, \lambda_{i,t-2}^a, \lambda_{i,t-1}^a$  and the prior scaling factor  $\lambda_{i,t}^p$  were used to estimate  $\lambda_{i,t}^f$  by the time smooth operator; namely,

$$\lambda_{i,t}^f = \frac{1}{M} \left( \sum_{j=t-M+1}^{t-1} \lambda_{i,j}^a + \lambda_{i,t}^p \right), (i = 1, \dots, N, j = t - M + 1, \dots, t - 1), (5)$$

Here,  $M$  is the time window of the smooth operator. In this study, a value of  $M = 4$  (hours) was chosen. According to the smooth operator, the ensemble mean values of  $\lambda_{i,t}^f$  depend on the ensemble mean of  $\lambda_{i,t-M+1}^a, \dots, \lambda_{i,t-2}^a, \lambda_{i,t-1}^a, \lambda_{i,t}^p$ , where the ensemble means of  $\lambda_{i,t}^p$  are all 1. After multiple iterations, the smooth operator can give comparatively good estimation for  $\lambda_{i,t}^f$  since anthropogenic emissions are stable at a certain time scale (Mijling et al., 2012). It is a compromise between prescribed prior emissions and letting the system propagate all observation information from one step to the next without any guidance (Peters et al., 2007), for the case  $M = 4$ .

The ensemble members of the emissions were calculated according to

$$\mathbf{E}_{i,t} = \lambda_{i,t} \mathbf{E}_t^p, (i = 1, \dots, N), (6)$$

where  $\mathbf{E}_{i,t}$  is the  $i$ th ensemble member of the emissions for each grid at time  $t$ ,  $\lambda_{i,t}$  represents the scaling factors and  $\mathbf{E}_t^p$  is the prescribed emission, which can be obtained from the emission inventories. It is noted that the correlations among the grid-points of the prior emissions depend on  $\lambda_{i,t}^p$ . These correlations may deviate far from the truth but we have no other suitable substitute. However, the correlations among the grid-points of the forecast emissions should be more or less close to the truth due to the appliance of the smooth operator after multiple iterations.

It is noted although the method is very similar to that used by Peters et al. (2007) and Peng et al. (2015) for CO<sub>2</sub> emission inversion, it is still of novelty for applications

in aerosol anthropogenic emissions. In Peters et al. (2007),  $\lambda_{i,t}^p$  were all 1. And only natural CO<sub>2</sub> emissions (i.e., biospheric and oceanic emissions) were assimilated at the ecological scale due to the ‘signal-to-noise’ problem. Thus, the uncertainty of anthropogenic and other CO<sub>2</sub> emissions were ignored. Besides, the framework is more advanced compared to our previous work. In Peng et al. (2015), in order to generate  $\lambda_{i,t}^p$ , a set of ensemble forecasts were performed from time  $t$  to  $t+1$  to produce the CO<sub>2</sub> concentration fields, forced by the prescribed net CO<sub>2</sub> surface fluxes with the previous assimilated concentration fields as initial conditions. That means that the ensemble forecast were performed twice in that DA system and it was time consuming. However, in order to save computing time, we used the chemical fields  $C_{i,t}^f$  available in the previous assimilation cycle to calculate  $\lambda_{i,t}^p$  in this work. Thus, WRF-Chem runs to forecast only once during a DA cycle.

## 2.2 Ensemble square root filter

The ensemble square root filter (EnSRF) algorithm was introduced by Whitaker and Hamill (2002) and its expansion to analyzing aerosol ICs was described by Schwartz et al. (2014). The traditional EnKF with perturbed observations (Evensen 1994) introduces sampling errors by perturbing the observations. In contrast to the traditional EnKF, the EnSRF (Whitaker and Hamill, 2002) and the Ensemble Adjustment Kalman Filter (EAKF, developed by Anderson, 2001) obviate the need to perturb the observations. The local ensemble Kalman filtering (LEKF), a kind of EnSRF, was presented by Ott et al. (2002, 2004). It was computationally more efficient compared to the traditional EnKF, since it simultaneously assimilates the observations within a spatially local volume independently. The local Ensemble Transform Kalman Filter (LETKF, Hunt, 2007) integrates the advantages of the Ensemble Transform Kalman Filter (ETKF, developed by Bishop et al., 2001) and the LEKF. The computational cost of LETKF is much lower than that of the original LEKF because the former does not require an orthogonal basis. Though LETKF has



more advantages, we still chose the same EnSRF as Schwartz et al. (2014) because we did not need to extend it to analyzing aerosol ICs, very similar to Schwartz et al. (2014).

Following the notation of Ide et al. (1997), given an  $m$ -dimensional background model forecast vector  $\mathbf{x}^b$ , a  $p$ -dimensional observation vector  $\mathbf{y}^o$  and an operator  $\mathbf{H}$  that converts the model state to the observation states, we expressed the variables as an ensemble mean (denoted by an over-bar) and a deviation from the mean (denoted by a prime). Thus, the ensemble mean  $\bar{\mathbf{x}}^a$  of the analyzed state  $\mathbf{x}^a$  and the deviations  $\mathbf{x}'^a$  from the ensemble mean are updated separately by

$$\bar{\mathbf{x}}^a = \bar{\mathbf{x}}^b + \mathbf{K}(\mathbf{y}^o - \mathbf{H}\bar{\mathbf{x}}^b), \quad (7)$$

$$\mathbf{x}'^a = \mathbf{x}'^b + \tilde{\mathbf{K}}(\mathbf{y}'^o - \mathbf{H}\mathbf{x}'^b), \quad (8)$$

where  $\mathbf{K}$  is the traditional Kalman gain matrix and  $\tilde{\mathbf{K}}$  is the gain used to update the deviations from the ensemble mean. These are given by

$$\mathbf{K} = \mathbf{P}^b \mathbf{H}^T (\mathbf{H} \mathbf{P}^b \mathbf{H}^T + \mathbf{R})^{-1}, \quad (9)$$

$$\begin{aligned} \tilde{\mathbf{K}} &= \mathbf{P}^b \mathbf{H}^T \left[ \left( \sqrt{\mathbf{H} \mathbf{P}^b \mathbf{H}^T + \mathbf{R}} \right)^{-1} \right]^T \left( \sqrt{\mathbf{H} \mathbf{P}^b \mathbf{H}^T + \mathbf{R}} + \sqrt{\mathbf{R}} \right)^{-1} \\ &= \left( \mathbf{1} + \sqrt{\mathbf{R} / (\mathbf{H} \mathbf{P}^b \mathbf{H}^T + \mathbf{R})} \right)^{-1} \mathbf{K}, \quad (10) \end{aligned}$$

where  $\mathbf{P}^b$  is the  $m * m$ -dimensional background error covariance matrix and  $\mathbf{R}$  is the  $p * p$ -dimensional diagonal observation error covariance matrix. In real applications,  $\mathbf{P}^b \mathbf{H}^T$  and  $\mathbf{H} \mathbf{P}^b \mathbf{H}^T$  will be approximated using the background ensemble; namely,

$$\mathbf{P}^b \mathbf{H}^T = \frac{1}{N-1} \sum_{i=1}^N \mathbf{x}'^b (\mathbf{H} \mathbf{x}'^b)^T \quad (11)$$

$$\mathbf{H} \mathbf{P}^b \mathbf{H}^T = \frac{1}{N-1} \sum_{i=1}^N \mathbf{H} \mathbf{x}'^b (\mathbf{H} \mathbf{x}'^b)^T. \quad (12)$$

In equations (11) and (12),  $N$  is the ensemble size.

Note that for the joint analysis of ICs and emissions, the state vector  $\mathbf{x}$  is the joint vector of the mass concentration  $\mathbf{C}$  and the emission scaling factor  $\boldsymbol{\lambda}$ , i.e.  $\mathbf{x} = [\mathbf{C}, \boldsymbol{\lambda}]^T$ . In this study, the state variables of the analysis of the ICs were the 15 WRF-Chem/GOCART aerosol variables, same as that reported by Schwartz et al. (2012). The state variables of the emission scaling factors include  $\lambda_{\text{PM}_{2.5}}$ ,  $\lambda_{\text{SO}_2}$ ,  $\lambda_{\text{NO}}$

and  $\lambda_{\text{NH}_3}$  and are described in section 2.3.1. After each ensemble analysis, the ensemble forecasts were performed with the corresponding models to advance  $\mathbf{C}$  and  $\lambda$  to the next analysis time.

In this work, a 50-member ensemble was chosen, following Schwartz et al. (2012) and Whitaker and Hamill (2002). Covariance localization forced EnSRF analysis increments to zero 1280 km from an observation in the horizontal and one scale height to reduce spurious correlations due to sampling error for all control variables, similar to Pagowski et al., (2012) and Schwartz et al., (2012, 2014). In addition, posterior (after assimilation) multiplicative inflation following Whitaker and Hamill (2012) was applied aiming to maintain ensemble spread for only the concentration analysis. The inflation factor  $\alpha = 1.2$  was chosen as Pagowski et al., (2012) and Schwartz et al., (2012, 2014). Additive or prior inflation was not employed. As for the emission scaling factor  $\lambda$ , the inflation was not used at this step.

## 2.3 Data assimilation system

### 2.3.1 State variables

As stated in section. 2.2, the state variables of the analysis of the ICs were the 15 WRF-Chem/GOCART aerosol variables. The  $\text{PM}_{2.5}$  observation operator was the same as that described by Schwartz et al. (2012) and expressed as

$$\mathbf{y}^f = \rho_d [\mathbf{P}_{25} + 1.375\mathbf{S} + 1.8(\mathbf{OC}_1 + \mathbf{OC}_2) + \mathbf{BC}_1 + \mathbf{BC}_2 + \mathbf{D}_1 + 0.286\mathbf{D}_2 + \mathbf{S}_1 + 0.942\mathbf{S}_2], \quad (13)$$

where  $\rho_d$  represents the dry air density, which is multiplied by the mixing ratios of aerosol species (in  $\mu\text{g}\cdot\text{kg}^{-1}$ ) to convert the units to  $\mu\text{g m}^{-3}$  for consistency with the observations.

From the perspective of the optimization of emissions, four species of emission scaling factors ( $\lambda_{\text{PM}_{2.5}}$ ,  $\lambda_{\text{SO}_2}$ ,  $\lambda_{\text{NO}}$  and  $\lambda_{\text{NH}_3}$ ) were also considered as the state variables of the DA system. Atmospheric inorganic aerosols are not only from the primary emissions, but also from secondary processes- chemical and thermodynamic transformations from the gas-phase precursors. Therefore, not only the primary sources of  $\text{PM}_{2.5}$ , but also the sources of the gas-phase precursors, need to be

optimized. In this study, the sources of  $\text{SO}_2$ ,  $\text{NO}_x$  and  $\text{NH}_3$  ( $\mathbf{E}_{\text{SO}_2}$ ,  $\mathbf{E}_{\text{NO}}$  and  $\mathbf{E}_{\text{NH}_3}$ ), which have a large impact on the distribution of  $\text{PM}_{2.5}$ , were also optimized in addition to the primary sources of  $\text{PM}_{2.5}$ . It is noted that for the optimization of the emission scaling factors,  $\mathbf{M}_{\text{SF}}$  serves as the forecast model and the observation operator reflects the combined information of emissions (in the format of  $\lambda$  in equation (6)), the physics and chemistry processes in WRF-Chem simulations and the transformation  $\text{PM}_{2.5}$  from model space to observation space (equation (13)).

The direct sources of  $\text{PM}_{2.5}$  include the unspciated primary sources of  $\text{PM}_{2.5}$   $\mathbf{E}_{\text{PM}_{2.5}}$ , sulfate  $\mathbf{E}_{\text{SO}_4}$ , nitrate  $\mathbf{E}_{\text{NO}_3}$ , organic compounds  $\mathbf{E}_{\text{org}}$  and elemental compounds  $\mathbf{E}_{\text{BC}}$ ; all of them are given in two modes (the nuclei and accumulation modes, represented as  $i$  and  $j$  in the subscripts respectively). The ratios between the nuclei and accumulation modes were the same as in the suggested emission process for National Emission Inventory in WRF-Chem (Freitas et al., 2011). The formula of sulfate and nitrate emissions in the model are as below:

$$\mathbf{E}_{\text{PM}_{2.5}i} : \mathbf{E}_{\text{PM}_{2.5}j} = 1 : 4, (14)$$

$$\mathbf{E}_{\text{SO}_4i} : \mathbf{E}_{\text{SO}_4j} = 1 : 4, (15)$$

$$\mathbf{E}_{\text{NO}_3i} : \mathbf{E}_{\text{NO}_3j} = 1 : 4, (16)$$

$$\mathbf{E}_{\text{SO}_4i} + \mathbf{E}_{\text{SO}_4j} = a * (\mathbf{E}_{\text{PM}_{2.5}i} + \mathbf{E}_{\text{PM}_{2.5}j} - \mathbf{E}_{\text{EC}} - \mathbf{E}_{\text{ORG}}), (17)$$

$$\mathbf{E}_{\text{NO}_3i} + \mathbf{E}_{\text{NO}_3j} = b * (\mathbf{E}_{\text{PM}_{2.5}i} + \mathbf{E}_{\text{PM}_{2.5}j} - \mathbf{E}_{\text{EC}} - \mathbf{E}_{\text{ORG}}), (18)$$

where  $\mathbf{E}_{\text{EC}}$  represents elemental carbon and  $\mathbf{E}_{\text{ORG}}$  organic compounds, and  $a = 0.074$  and  $b = 0.038$  were chosen based on the internal emissions and observational data. In the DA process, the first 6 species of direct sources of emissions ( $\mathbf{E}_{\text{PM}_{2.5}i}$ ,  $\mathbf{E}_{\text{PM}_{2.5}j}$ ,  $\mathbf{E}_{\text{SO}_4i}$ ,  $\mathbf{E}_{\text{SO}_4j}$ ,  $\mathbf{E}_{\text{NO}_3i}$ , and  $\mathbf{E}_{\text{NO}_3j}$ ), which may have larger uncertainties in heavy polluted events, were updated according to the variation of  $\lambda_{\text{PM}_{2.5}}$ .  $\mathbf{E}_{\text{PM}_{2.5}i}$  and  $\mathbf{E}_{\text{PM}_{2.5}j}$  were directly updated according to the variation in  $\lambda_{\text{PM}_{2.5}}$ . The emissions ( $\mathbf{E}_{\text{SO}_4i}$ ,  $\mathbf{E}_{\text{SO}_4j}$ ,  $\mathbf{E}_{\text{NO}_3i}$  and  $\mathbf{E}_{\text{NO}_3j}$ ) were also updated according to the variations in  $\mathbf{E}_{\text{PM}_{2.5}i}$  and  $\mathbf{E}_{\text{PM}_{2.5}j}$ .

$E_{EC}$  and  $E_{ORG}$  of the anthropogenic emissions were not assimilated, which is a limitation in this work. Besides, emissions of dust and sea salt were not assimilated. It is true that these emissions are also important for the atmosphere aerosol. The reason we did not assimilate  $E_{EC}$  and  $E_{ORG}$  is that only the  $PM_{2.5}$  measurements are used in this DA experiment. However, the sources of the aerosols (especially organic aerosols) are so complex that our knowledge of their formation mechanisms is far from clear. Though it is technically possible to have all emissions assimilated, with such limited observations adding more control variables would cause much more uncertainties in the system which might lead to unreasonable analysis.

### 2.3.2 Procedure for the DA system

Figure 2 (b) shows the workflow of the DA system. The steps in this workflow are as follows.

(1) The persistence forecasting operator  $M_{SF}$  is applied to forecast the background fields of the emission scaling factors  $\lambda_{PM_{2.5}}^f$ ,  $\lambda_{SO_2}^f$ ,  $\lambda_{NO}^f$  and  $\lambda_{NH_3}^f$ . The forecast chemical fields of  $P_{25}$ ,  $SO_2$ ,  $NO$  and  $NH_3$  of the previous assimilation cycle are used to create the prior emission scaling factors  $\lambda_{PM_{2.5}}^p$ ,  $\lambda_{SO_2}^p$ ,  $\lambda_{NO}^p$  and  $\lambda_{NH_3}^p$ . The background scaling factors are then generated using equation (5).

(2) The ensemble members of the emissions,  $E_{PM_{2.5}i}^f$ ,  $E_{PM_{2.5}j}^f$ ,  $E_{SO_2}^f$ ,  $E_{NO}^f$  and  $E_{NH_3}^f$ , are prepared according to equation (6). The corresponding emissions of  $E_{SO_4i}^f$ ,  $E_{SO_4j}^f$ ,  $E_{NO_3i}^f$  and  $E_{NO_3j}^f$  are obtained based on equations (15–18). Other inorganic species of the anthropogenic emission, such as  $E_{EC}$  and  $E_{ORG}$ , are not perturbed for WRF-Chem, which is a limitation of this manuscript. However, other anthropogenic emissions, such as  $E_{PM_{2.5}}$ ,  $E_{SO_4}$  and  $E_{NO_3}$ , are much larger than  $E_{EC}$  and  $E_{ORG}$  in most area of China, and the ensemble spreads of the aerosol concentrate largely dependent on the uncertainties of those anthropogenic emissions. Besides, model errors raised from the meteorology, the emission and the chemical model itself are compensated to some extent through the use of multiplicative inflation. In other words, the ensemble spread of the concentrations can be kept at a certain level though  $E_{EC}$

and  $E_{\text{ORG}}$ , are not perturbed.

Natural emissions, such as dust and sea salt emissions were not perturbed explicitly when the forecast emissions were generated. However, emissions of dust and sea salt were parameterized within the GOCART model (Chin et al., 2002). Within the DA system, varying meteorology across the members implicitly perturbed dust and sea salt emissions.

(3) Forced by the changed emissions ( $E_{\text{PM}_{2.5}\text{i}}$ ,  $E_{\text{PM}_{2.5}\text{j}}$ ,  $E_{\text{SO}_2}$ ,  $E_{\text{NO}}$ ,  $E_{\text{NH}_3}$ ,  $E_{\text{SO}_4\text{i}}$ ,  $E_{\text{SO}_4\text{j}}$ ,  $E_{\text{NO}_3\text{i}}$  and  $E_{\text{NO}_3\text{j}}$  were substituted by  $E_{\text{PM}_{2.5}\text{i}}^{\text{f}}$ ,  $E_{\text{PM}_{2.5}\text{j}}^{\text{f}}$ ,  $E_{\text{SO}_2}^{\text{f}}$ ,  $E_{\text{NO}}^{\text{f}}$ ,  $E_{\text{NH}_3}^{\text{f}}$ ,  $E_{\text{SO}_4\text{i}}^{\text{f}}$ ,  $E_{\text{SO}_4\text{j}}^{\text{f}}$ ,  $E_{\text{NO}_3\text{i}}^{\text{f}}$  and  $E_{\text{NO}_3\text{j}}^{\text{f}}$ ; the other emissions such as  $E_{\text{EC}}$  and  $E_{\text{ORG}}$  remained unchanged), WRF-Chem is run again to forecast the chemical fields  $\rho^{\text{f}}$  with the updated chemical fields of the previous assimilation cycle as the ICs. The state variables, i.e., 15 aerosol species and four scaling factors, are then prepared.

(4) The model-simulated  $\text{PM}_{2.5}$  concentration at the observation space is then calculated via equation (13). At this time, the state vector  $\mathbf{x}^{\text{f}} = [\mathbf{C}^{\text{f}}, \boldsymbol{\lambda}^{\text{f}}]^{\text{T}}$  was prepared.

(5) In the assimilation step, the state variables, the concentrations of 14 defined aerosol species and a 15th unspciated aerosol, and the four species of emission scaling factors  $\lambda_{\text{PM}_{2.5}}^{\text{f}}$ ,  $\lambda_{\text{SO}_2}^{\text{f}}$ ,  $\lambda_{\text{NO}}^{\text{f}}$  and  $\lambda_{\text{NH}_3}^{\text{f}}$ , were optimized through EnSRF.

(6) After the assimilation step, the optimized emissions ( $E_{\text{PM}_{2.5}\text{i}}^{\text{a}}$ ,  $E_{\text{PM}_{2.5}\text{j}}^{\text{a}}$ ,  $E_{\text{SO}_2}^{\text{a}}$ ,  $E_{\text{NO}}^{\text{a}}$ ,  $E_{\text{NH}_3}^{\text{a}}$ ,  $E_{\text{SO}_4\text{i}}^{\text{a}}$ ,  $E_{\text{SO}_4\text{j}}^{\text{a}}$ ,  $E_{\text{NO}_3\text{i}}^{\text{a}}$  and  $E_{\text{NO}_3\text{j}}^{\text{a}}$ ) were calculated according to equations (6, 15–18) using the optimized scaling factors ( $\lambda_{\text{PM}_{2.5}}^{\text{a}}$ ,  $\lambda_{\text{SO}_2}^{\text{a}}$ ,  $\lambda_{\text{NO}}^{\text{a}}$  and  $\lambda_{\text{NH}_3}^{\text{a}}$ ).

### 3. $\text{PM}_{2.5}$ observation data and errors

Hourly averaged surface  $\text{PM}_{2.5}$  observations from the Ministry of Environmental Protection of China were assimilated. Figure 1 shows the locations of 77 measurement sites used for the  $\text{PM}_{2.5}$  assimilation experiment and 77 independent sites used for forecast verification. The observation sites spanned most of central and eastern China and were primarily located in urban and suburban areas.

The observation error covariance matrix  $\mathbf{R}$  in equation (9) includes contributions from measurement and representation errors. Similar to the work of Schwartz et al. (2012), the measurement error  $\varepsilon_0$  is defined as  $\varepsilon_0 = 1.5 + 0.0075 * \Pi_0$ , where  $\Pi_0$  denotes the observational values for  $\text{PM}_{2.5}$  ( $\mu\text{g m}^{-3}$ ). Thus, higher  $\text{PM}_{2.5}$  values were associated with larger measurement errors. Following Elbern et al. (2007) and Pagowski et al. (2010), Schwartz et al. (2012), the representativeness error  $\varepsilon_r$  depends on the resolution of the model and the characteristics of the observation locations and is calculated as  $\varepsilon_r = r\varepsilon_0\sqrt{\Delta x/L}$ , where  $r$  is an adjustable parameter (here,  $r = 0.5$ ),  $\Delta x$  is the grid spacing (here, 40.5 km), and  $L$  is the radius of influence of an observation (here,  $L$  was set to 3 km following Elbern et al. (2007), since we do not know the station type that used in this work). The total  $\text{PM}_{2.5}$  error ( $\varepsilon_t$ ) is defined as  $\varepsilon_t = \sqrt{\varepsilon_0^2 + \varepsilon_r^2}$ . The observation errors are assumed to be uncorrelated so that  $\mathbf{R}$  is a diagonal matrix.

The  $\text{PM}_{2.5}$  observations were subject to quality control to ensure data reliability before DA.  $\text{PM}_{2.5}$  values larger than  $800 \mu\text{g m}^{-3}$  are classified as unrealistic and were not assimilated; observations with the ensemble mean of the first guess departure exceeding  $100 \mu\text{g m}^{-3}$  are also omitted. The numbers of the observations were about 17700. Among them 8 observations were discarded because they were larger than  $800 \mu\text{g m}^{-3}$  and 243 (around 1.5%) were discarded due to the latter reasons.

#### 4. Experimental design

Two parallel experiments were performed to evaluate the impact of  $\text{PM}_{2.5}$  DA on the analyses and forecasts of aerosols over China: an assimilation experiment and a control experiment. Both experiments used identical WRF-Chem settings and physical parameterizations.

##### 4.1 Spin-up ensemble forecast with perturbed Initial and boundary conditions

The initialization and spin-up procedures were identical to those reported by Schwartz et al. (2014). The ICs and lateral boundary conditions (LBCs) for the

meteorological fields were provided by the National Centers for Environmental Prediction Global Forecast System (GFS).

The initial meteorological fields were created at 0000 UTC 1 October 2014 by interpolating the GFS analyses onto the model domain. The 50 ensemble members were then generated by adding Gaussian random noise with a zero mean and static background error covariances (Torn et al., 2006) to the temperature, water vapor, velocity, geopotential height and dry surface pressure fields. The ICs of each member were zero in the initial aerosol fields, representing clean conditions as described by Liu et al. (2011).

The LBCs for the meteorological fields were then interpolated from the GFS analyses from 0000 UTC 1 October 2014 to 0000 UTC 16 October 2014 and perturbed similarly to the initial fields at 0000 UTC 1 October 2014. The aerosol LBCs of each member for all experiments were idealized profiles embedded within the WRF/Chem model.

Fifty-member emissions were created by adding random noise to the anthropogenic emissions, same as reported by Schwartz et al. (2014),

$$\mathbf{E}_{ip}^*(\eta, t) = \mathbf{E}_p(\eta, t) + \mathbf{W}_{ip}\sigma_p^E(\eta, t)$$

where  $\mathbf{E}_{ip}^*(\eta, t)$  is the  $i$ th ensemble member for the  $p$ th emissions variable at the  $\eta$ th grid point and the  $t$ th hour,  $\mathbf{E}_p$  is the unperturbed emissions. The term  $\sigma_p^E$  is the standard deviation of all  $\mathbf{E}_p$  values and in the horizontally adjacent points of grid box  $\eta$  at and within 2 h of  $t$ .  $\mathbf{W}$  is a weight that was randomly drawn from a standard Gaussian distribution and varied for each ensemble member and variable but was spatially and temporally constant. No correlations between emissions variables were considered, which is a limitation of this approach. For possible negative perturbed emissions, they were set as  $\mathbf{E}_{ip}^*(\eta, t) = 0.001 * \mathbf{E}_p(\eta, t)$ . This will increase the prescribed emissions more or less. However, only very few data were negative. So, this influence can be negligible.

Before the first DA cycle, a 50-member ensemble of four-day WRF-Chem

forecasts was performed from 0000 UTC 1 October to 2300 UTC 4 October 2014 using the perturbed ICs at 0000 UTC 1 October 2014, the corresponding perturbed LBCs and the emissions. Then a 50-member ensemble aerosol forecasts at 0000 UTC 5 October 2014 were produced.

## 4.2 Assimilation experiments

Two DA experiments were performed. One was the pure assimilation of chemical ICs (hereafter expC), the others was the joint adjustment of chemical ICs and source emissions (hereafter expJ). Both DA experiments had same settings except for the emissions. They were conducted from 0000 UTC 5 October 2014 to 0000 UTC 16 October 2014. The assimilation cycle interval was 1 h.

In the first DA cycle in expJ, the first 50 ensemble chemical fields were drawn from the WRF-Chem ensemble forecasts valid at 0000 UTC 5 October 2014, as described in section 4.1. Using the ensemble aerosol forecasts, the prior emission scaling factors  $\lambda_{i,t}^p$  at 2300 UTC 4 October 2014 were calculated.  $\lambda_{i,t}^p$  were used directly as  $\lambda_{i,t}^f$  for the first 5 assimilation cycles (after 5 assimilation cycles, the system has been initialized, all future scaling factors could be created using the persistence forecasting operator  $\mathbf{M}_{SF}$ ). Then, the state vector  $\mathbf{x}^f = [\mathbf{C}^f, \lambda^f]^T$  was prepared. And after that, the DA cycle started.

In expC, the first chemical fields were also drawn from the WRF-Chem ensemble forecasts valid at 0000 UTC 5 October 2014. Then, the state vector  $\mathbf{x}^f = [\mathbf{C}^f]^T$  was prepared and the DA cycle started.

At the WRF-Chem forecast step of the subsequent assimilation cycles for both experiments, the ICs for the chemical variables of each member were drawn from the updated chemical fields of the previous cycle. The aerosol LBCs of each member for all experiments were idealized profiles embedded within the WRF/Chem model. As for the meteorological ensemble fields, the LBCs were prepared in advance as depicted in section 4.1; the ICs of each member of the meteorological fields were drawn from the forecast meteorological fields of the previous cycle before



re-centering with the GFS analysis because we do not do meteorological analysis:

$$\boldsymbol{\pi}_{i_{\text{new}}} = \boldsymbol{\pi}_i + (\boldsymbol{\pi}_{\text{GFS}} - \bar{\boldsymbol{\pi}}), (18)$$

where  $\boldsymbol{\pi}_i$  is the  $i$ th member of the forecast meteorological fields of the previous cycle,  $\bar{\boldsymbol{\pi}}$  is the ensemble mean of the forecast meteorological fields of the previous cycle,  $\boldsymbol{\pi}_{\text{GFS}}$  is the meteorological field interpolated from the GFS analyses and  $\boldsymbol{\pi}_{i_{\text{new}}}$  is the new meteorological field used as the IC in WRF-Chem in the next cycle.

As stated in the first paragraph in this section, the settings of expC were the same as those in expJ except for the emissions. In expJ, the ensemble anthropogenic emissions were generated by using emission scaling factors. While in expC, the ensemble anthropogenic emissions were prepared by adding random noise, as stated in 4.1.

### 4.3 Control experiment

The control experiment was conducted for the same period as the assimilation experiment and the simulation cycle period was 1 h, as in the assimilation experiment. The first initial chemical fields were extracted from the ensemble mean valid at 0000 UTC 5 October 2014. In the subsequent simulation process, the ICs for the chemical fields were from the previous cycle's 1-h forecast. The LBCs and ICs for the meteorological fields were updated by interpolating the GFS analyses. The emissions were the prescribed emissions  $\mathbf{E}_t^p$  without any perturbation.

## 5. Results

Statistics for both expJ and expC were computed using the ensemble mean prior (background) and posterior (analysis) fields (average of the 50-member ensemble). The ensemble performances were first examined. Output from the first day of the cycling DA configurations was excluded from all verification statistics to allow the ensemble fields to “spin up” from the initial ensemble.

As the measurement coverage is an important factor that may determine the performance in DA, we primarily focused our attention on the results from three

sub-regions with comparatively dense observational coverage (Figure 1): the Beijing–Tianjin–Hebei region (JJJ, 12 stations); the Yangtze River delta (YRD, 24 stations); and the Pearl River delta (PRD, 9 stations).

### 5.1 Ensemble performance

It is important to assess the ensemble performance for an ensemble-based DA system. In a well-calibrated system, a comparison of the prior ensemble mean root-mean-square error (RMSE) with respect to the observations should equal the prior “total spread” (square root of the sum of ensemble variance and observation error variance) (Houtekamer et al., 2005). Figure 3 shows the time series for the prior ensemble mean RMSE and the total spread for  $\text{PM}_{2.5}$  aggregated over all observations in the three sub-regions for expJ. It indicates that the magnitudes of both the total spread and the RMSE were influenced by the diurnal cycle and heavy air pollution. Almost all the total spreads were smaller than the RMSE, showing an insufficient spread of  $\text{PM}_{2.5}$  ensemble forecasts, which is especially evident for heavy polluted period with much larger RMSEs. For expC, the characteristics of the prior ensemble mean RMSE and the total spread for  $\text{PM}_{2.5}$  were very similar to that for the joint DA experiment.

The magnitudes of the ensemble spread of the emission scaling factors of the joint DA experiment were important for emission inversion. They were very stable throughout the ~10 day experiment period, which indicates that  $\mathbf{M}_{\text{SF}}$  can generate stable artificial data to generate the ensemble emissions. For  $\lambda_{\text{PM}_{2.5}}^f$ , they ranged from 0.25 to 1 in most model area. Figure 3d shows the area-averaged time series extracted from the ensemble spread of  $\lambda_{\text{PM}_{2.5}}^f$ . It shows that the ensemble spread was stably distributed around 0.5, which indicates that the uncertainty of the ensemble emissions was about 50%.

### 5.2 Impact on aerosol ICs

To evaluate quantitatively the impact of the ensemble assimilation system on the ICs, the mean errors (bias), RMSEs and correlation coefficient (CORR) of the assimilation

experiment and the control run were first analyzed. These statistics were calculated against independent observations over all the analyses from 6 to 16 October 2014. Table 1 shows that the bias magnitudes of the control run were 15.9 and 20.6  $\mu\text{g m}^{-3}$  for the YRD and the PRD, respectively, suggesting a significant overestimation of the WRF-Chem aerosol mass in these two sub-regions. However, a significant underestimation of the aerosol mass occurred in the JJJ region, where the model bias was  $-18.0 \mu\text{g m}^{-3}$ . The RMSEs of the control run were 81.6, 30.6 and 31.8  $\mu\text{g m}^{-3}$  for the JJJ, YRD and PRD regions, respectively. After assimilation, the statistics showed an apparent improvement and the magnitude of the bias and the RMSE decreased for both DA experiment. For expJ, both the maximum bias and the RMSE were obtained in the JJJ region, and were  $-10.3$  and  $66.9 \mu\text{g m}^{-3}$ , respectively. The CORR increased from 0.79, 0.60, and 0.62 to 0.83, 0.85, and 0.80 for the JJJ, YRD and PRD, respectively. The statistics of expC were very similar to those of expJ. The bias and the RMSE in the JJJ region were  $-12.2$  and  $64.0 \mu\text{g m}^{-3}$ , respectively. And the CORR were 0.85, 0.80, and 0.80 for the JJJ, YRD and PRD, respectively. These results indicate that the initial  $\text{PM}_{2.5}$  fields can be adjusted efficiently by the EnSRF.

Then the analysis increments (i.e.  $\bar{\mathbf{x}}^a - \bar{\mathbf{x}}^b$ ) were investigated to show the direct impact of  $\text{PM}_{2.5}$  DA. They are determined by both the observation increments and the relative magnitudes of the forecast error and the observation error, based on Equation (7). From Figure 4(a), (e) and (f), the increments of both assimilation experiments were distributed around the observations as expected. However, the impact of assimilating  $\text{PM}_{2.5}$  observations was not limited to the areas where observations were located, observations information was also transported to other areas through the WRF-Chem forecast. Besides, the ensemble forecasts also partly contributed to the spatial distribution of the  $\text{PM}_{2.5}$  mass. Therefore, the spatial distributions of the  $\text{PM}_{2.5}$  mass in both assimilation experiments were significantly different from the control run (see Figure 4(b), (c) and (d)), which suggest that assimilation  $\text{PM}_{2.5}$  observations impacts greatly on the aerosol ICs. The  $\text{PM}_{2.5}$  mass magnitude of both assimilation experiments were smaller than that of the control run at the lowest model level in the YRD, the PRD and in central China. Conversely, positive differences (analysis minus

control) were gained in the JJJ region and in northeast China. These indicated the reduction of the overestimation or underestimation of the WRF-Chem simulation over these regions with data assimilation.

### 5.3 Impact on emissions

To determine the impact of assimilating  $\text{PM}_{2.5}$  observations on the chemical emissions, we analyzed the area-averaged time series extracted from the forecast emission scaling factors, the optimized emission scaling factors, the prior emissions and the optimized emissions. Figure 5 shows that  $\lambda_{\text{PM}_{2.5}}^f$  were changed along with  $\lambda_{\text{PM}_{2.5}}^a$ . This indicates that observation information ingested from the previous observations was incorporated through the usage of the time smooth operator.

Figure 5 also shows that although the prior emissions  $E_{\text{PM}_{2.5}}^p$  had no diurnal variation when the experiments were designed, the optimized  $\text{PM}_{2.5}$  scaling factor,  $\lambda_{\text{PM}_{2.5}}^a$ , showed an obvious variation with time, as did the optimized unspiciated primary sources of  $\text{PM}_{2.5}$ ,  $E_{\text{PM}_{2.5}}^a$ . Moreover, the values of  $\lambda_{\text{PM}_{2.5}}^a$  were  $<1$  at almost all times in the YRD and PRD, which resulted that the analyzed emission  $E_{\text{PM}_{2.5}}^a$  were lower than the prior  $\text{PM}_{2.5}$  emissions  $E_{\text{PM}_{2.5}}^p$ . In the YRD, the prior  $E_{\text{PM}_{2.5}}^p$  was about  $0.127 \mu\text{g m}^{-2} \text{s}^{-1}$  over all hours. After assimilation, the time-averaged optimized  $E_{\text{PM}_{2.5}}^a$  decreased to  $0.107 \mu\text{g m}^{-2} \text{s}^{-1}$ , about 15.6% lower than the prior value. In the PRD, the prior  $E_{\text{PM}_{2.5}}^p$  was about  $0.10 \mu\text{g m}^{-2} \text{s}^{-1}$ . The time-averaged optimized  $E_{\text{PM}_{2.5}}^a$  decreased to  $0.066 \mu\text{g m}^{-2} \text{s}^{-1}$ , leading to a decrease of 35.0%. However, larger values for the optimized  $E_{\text{PM}_{2.5}}^a$  were obtained in the JJJ region in three periods, from 1600 UTC 6 October to 0000 UTC 8 October, from 1600 UTC 9 October to 0000 UTC 10 October, and from 1600 UTC 13 October to 0000 UTC 15 October as a result of the increased optimized scaling factor  $\lambda_{\text{PM}_{2.5}}^a$ . This may have been caused by the burning of crop residues during harvesting in this region (Li et al., 2016), which was not taken into account in the prior emissions. However, the  $\text{PM}_{2.5}$  measurements network was still spatially sparse and heterogeneous in this work. Almost all measurements were located in the city and no data available in the rural.

Meanwhile, the crop residues burning always occur in the rural region. Therefore, the PM<sub>2.5</sub> measurements network can only capture the burning information a few hours later. Hence, although the system is able to detect the emission changes caused by burning events, the time that the system started to show increased scaling factors might be not accurate enough (may shift a few hours later). Maybe a Kalman smoother would have been a better system to solve this problem.

The NO, SO<sub>2</sub> and NH<sub>3</sub> emissions were all adjusted to some extent by our DA approach. The NO emissions increased by 41.3, 43.7 and 20.3% in the JJJ, YRD and PRD regions, respectively. The SO<sub>2</sub> emissions increased by 16.3, 10.0 and 18.3% and the NH<sub>3</sub> emissions increased by 16.7, 7.8 and 7.5% in the JJJ, YRD and PRD regions, respectively.

Figure 6 shows the spatial distribution of the time-averaged scaling factors  $\lambda_{\text{PM}_{2.5}}^a$  at the lowest model level over all hours from 6 to 16 October 2014, since the emissions at higher levels were so small that the impact of assimilating PM<sub>2.5</sub> observations was negligible. Figure 7 shows the distribution of  $E_{\text{PM}_{2.5}}^p$  and the time-averaged differences between the ensemble mean of the assimilation and the prior values.

These patterns are consistent with those in Figure 5. Negative differences were obtained in most areas of the YRD and PRD, indicating that the PM<sub>2.5</sub> DA primarily decreased the PM<sub>2.5</sub> emissions. Conversely, positive differences were obtained in South Hebei, North Henan and Southeast Shanxi provinces, indicating that DA increased the PM<sub>2.5</sub> emissions.

As the economy in China has developed, the spatiotemporal distribution of emissions has changed as a result of changes in energy consumption, the structure of the energy market and advances in technology. Therefore although this inventory of emissions may have correctly described anthropogenic emissions in 2006 when it was constructed, it is not representative of the anthropogenic emissions in 2014. Theoretically, the assimilated emissions should reduce the uncertainty in the prior emissions as a result of the application of observations. Different from the situations

that standard national emission inventories were reported by government in USA, European or other countries, the rapid economic development and complexity of emission sources in China lead to large uncertainties in the current emission inventories even for the latest version. Thus it's impossible for us to conduct the direct evaluation on emissions.

Although we had no direct emission observations to evaluate the analyzing emissions, which was a challenging to many emission inversion research teams (e.g. Tang et al, 2011; Miyazaki et al., 2012; Ding et al., 2015; McLinden et al., 2016; etc.), the improvement of emissions can be verified in terms of two aspect, the diurnal variation and the location of increased emissions. The diurnal variation in the assimilated emissions verified this statement to some extent. Especially in the PRD and YRD,  $E_{PM_{2.5}}^a$  in the daytime were always larger than those in the night, which agreed well with Olivier et al. (2003), the WRAP (2006) and Wang et al. (2010). In addition, the locations of the larger values for the optimized  $E_{PM_{2.5}}^a$  in the JJJ region was in good agreement with the place of the crop residues burning traced by the environmental satellite of China. There were 10, 231, 37 and 3 crop residue burning spots in Hebei, Henan, Shandong and Shanxi province respectively from 5 to 11 October 2014 and 7, 20, 5 and 21 respectively from 12 to 18 October 2014 (Weekly Crop Residue Burning Monitoring Report traced by Environmental Satellite, 2015a, 2015b).

However, the analyzing emissions are only a mathematical optimum. They are influenced greatly by the model errors and the observation errors. In addition, only surface  $PM_{2.5}$  observations were applied in this work, which may lack abundant constraint on the sources of the secondary aerosol precursors. More observations are needed to obtain reliable emissions for the sources of the gas-phase precursors.

#### 5.4 Verification of aerosol forecasting

For the assimilation experiment, 48-h forecasts were performed at each 0000 UTC from 6 to 16 October 2014 with the hourly forecast output for both assimilation experiments. For the verification forecasting experiment for expJ (hereafter fcJ), the

ensemble mean of the analyzed ICs and emissions of expJ were used in this longer-range model forecast. For the verification forecasting experiment for expC (hereafter fcC), the ensemble mean of the analyzed ICs of expC and the prescribed anthropogenic emissions were used.

In order to get a more visualized picture of the impact of DA for both assimilation experiments, time series of the hourly  $PM_{2.5}$  extracted from the analysis (AN), the control run (CT) and the hourly output of 48-h forecast (fc24 for the first day forecast and fc48 for the second day forecast) were compared with the observations (OBS) for three megacities Beijing, Shanghai and Guangzhou, respectively (Figure 8). As expected, the time series of the analysis (also the background) were consistent with the observations. The control run showed large deviations from the observations, especially in Shanghai and Guangzhou. Benefit from DA on both the first day and the second day forecasts can be clearly seen.

The bias and the RMSE of the surface  $PM_{2.5}$  forecasts as a function of forecast range was then calculated against the independent observations for the three sub-regions (Figure 9). Both the bias and the RMSEs of the control run were characterized by the diurnal cycle in the YRD and PRD. The largest errors were seen at 2100 UTC in the YRD (about  $29 \mu g \cdot m^{-3}$  for bias and  $37 \mu g \cdot m^{-3}$  for RMSEs) and at 2300 UTC in the PRD (about  $36 \mu g \cdot m^{-3}$  for bias and  $41 \mu g \cdot m^{-3}$  for RMSEs), likely indicating significant systematic forecast errors at these times. From 0300 to 0900 UTC, the bias (about  $1 \mu g \cdot m^{-3}$  in the YRD and  $-5 \mu g \cdot m^{-3}$  in the PRD) and the RMSE values (about  $14 \mu g \cdot m^{-3}$  in the YRD and  $16 \mu g \cdot m^{-3}$  in the PRD) were much smaller than at other times in both the YRD and PRD, showing that WRF-Chem performed well during this period. However, in the JJJ region, the bias (about  $-20 \mu g \cdot m^{-3}$ ) and the RMSEs (about  $50 \mu g \cdot m^{-3}$ ) were always large as a result of a heavy pollution event. After assimilation, both the magnitude of the bias and the RMSEs decreased sharply. Especially in in YRD and PRD, most bias ranged from  $-5$  to  $5 \mu g \cdot m^{-3}$  and most RMSEs ranged from 11 to  $14 \mu g \cdot m^{-3}$ , further indicating that DA greatly affected the ICs.

The improvements in the surface  $PM_{2.5}$  forecasts by the joint adjustment of the

ICs and emissions were dramatic in the YRD and PRD for expJ. Large reduction of the magnitude of the bias and the RMSEs due to assimilation can be seen for almost the entire 48-h forecast range. From 10- to 23-h and from 34- to 47-h, in particular, the relative reduction in RMSE was about 37.5%. However, the DA impact was much smaller for 3- to 9-h forecast ranges, which are at daytime of the first day forecast. This may be because WRF-Chem performed sufficiently well during this period and therefore the further improvement was more difficult. From the perspective of the DA impact, the differences between the optimized PM<sub>2.5</sub> emissions and the prior emissions from 0000 to 0700 UTC each day were always smaller than those for other periods. In addition, the improvements were nearly negligible from 27- to 33-h, the daytime of the second day forecast, suggesting that the benefit gained from adjusting the ICs decreased progressively and eventually disappeared with model integration. Nevertheless, attributed greatly to the large adjustment of chemical emissions, substantial improvements were still achieved from 34- to 47- h. These results revealed that joint adjustment of the ICs and emissions can improve surface PM<sub>2.5</sub> forecasts up to 48 h in the YRD and PRD.

As for expC, it seemed that large improvements in the surface PM<sub>2.5</sub> forecasts were gained through the adjustment of the ICs in PRD from 10- to 23-h and from 34- to 47-h. Large reduction of the magnitude of the bias and the RMSEs due to assimilation can be seen during this period. The relative reduction in RMSE ranged from 25% to 37.5%. However, the forecasts deviated much from the observations for 3- to 9-h and 27- to 33-h forecast ranges. One of the reason may be that the adjustment of the ICs decreased the analysis field too much on the whole since the WRF-Chem forecast aerosol mass was systematically overestimated in PRD (see Figure 4, Figure 8f and Figure 9e). While this aerosol mass overestimation might be also due to the possibly overestimated emissions in some time periods (not all-day long) which are not corrected in the simulation. So the over-adjusted ICs compensated the unadjusted emissions in some period but also lead to the negative biases for the periods when emission is not overestimated or underestimated. The other factor was the diurnal variation. It is very clear that PM<sub>2.5</sub> mass gradually decreased with time



from 0000 UTC to 0008 UTC and then obtained the smallest value. After that it increased with time from 0009 UTC to 0023 UTC obtained the largest value at about 0000 UTC. Both reasons led to the systematically underestimation of  $PM_{2.5}$  mass of fcC from 3- to 9-h and from 27- to 33-h, though maybe the aerosol ICs were very close to the observations. Therefore, both the magnitude of the bias and the RMSEs of the fcC were larger than those of the control run. In addition,  $PM_{2.5}$  forecasts of the fcC were benefit much from the diurnal variation and the adjustment of the ICs from 10- to 23-h and from 34- to 47-h. As a consequence, the magnitude of the corresponding bias and the RMSEs of the fcC were smaller than those of the control run. Similar statics characteristics were also gained in YRD. But the improvements were comparatively small from 10- to 23-h and from 34- to 47-h. However, the performance of fcJ was always much better than that of the fcC for almost the entire 48-h forecast range in the PRD and YRD.

Both DA systems did not perform as well in the JJJ region as in the YRD and RRD and relatively smaller improvements were achieved in the first 24-h forecast. One possible reason for this result may be systematic errors due to chemistry mechanism in WRF-Chem. The sources of the aerosols are so complex that our knowledge of their formation mechanisms is far from clear and large uncertainties still exist in the model simulations. Chemical transport models have a tendency to underestimate PM concentrations, especially during episodes of heavy pollution (Denby et al., 2007) due to some missing reactions (Wang et al., 2014; Zhang et al., 2015, Zheng et al., 2015; Chen et al., 2016). As a result, a large bias may be obtained in forecasts of heavy pollution given the ICs and emission inventories achieved from the joint assimilation. Another reason may be the sparse coverage of measurements. There were only 12 sites in the JJJ region (Figure 1) and the measurement coverage was much sparser than in the YRD or PRD.

## 6. Summary

The EnSRF algorithm was extended to adjust the chemical ICs and the primary and precursor emissions to improve forecasts for surface  $PM_{2.5}$ . This system was

709 applied to assimilate hourly surface  $\text{PM}_{2.5}$  measurements from 5 to 16 October 2014  
710 over China. To evaluate the effectiveness of DA, 48-h forecasts were performed using  
711 the optimized ICs and emissions, together with a control experiment without DA.  
712 Besides, the experiment of pure assimilation chemical ICs and the corresponding 48-h  
713 forecasts experiment were also performed for comparison. The results indicated that  
714 the forecasts with the optimized ICs and emissions performed much better than the  
715 control simulations. Large improvements were achieved for almost all the 48-h  
716 forecasts, particularly in the YRD and PRD. However, relatively smaller  
717 improvements were achieved in the first 24-h forecast in the JJJ region, which may be  
718 attributed to the sparse measurement coverage and the deficiencies in the model  
719 system for forecasting heavy pollution. Comparing to the forecasts with only the  
720 optimized ICs, the forecasts with the joint adjustment were always much better for  
721 almost all the forecasts in the PRD and YRD. However, In the JJJ region, they were  
722 very similar.

723 This study represents the first step in the simultaneous optimization of chemical  
724 ICs and emissions and only surface  $\text{PM}_{2.5}$  measurements were assimilated. In future  
725 work, gas-phase observations of  $\text{SO}_2$ ,  $\text{NO}_2$  and CO will be used to further improve the  
726 performance of this DA system.

## References

- Anderson, J.L.: An Ensemble Adjustment Kalman Filter for Data Assimilation, *Mon. Weather Rev.*, 129, 2884–2903, 2001.
- Adhikary, B., Kulkarni, S., Dallura, A., Tang, Y., Chai, T., Leung, L. R., Qian, Y., Chung, C. E., Ramanathan, V., and Carmichael, G. R.: A regional scale chemical transport modeling of Asian aerosols with data assimilation of AOD observations using optimal interpolation technique, *Atmos. Environ.*, 42, 8600–8615, doi:10.1016/j.atmosenv.2008.08.031, 2008.
- Barbu, A. L., Segers, A. J., Schaap, M., Heemink, A.W., and Builtjes, P. J. H.: A multi-component data assimilation experiment directed to sulphur dioxide and sulphate over Europe, *Atmos. Environ.*, 43, 1622–1631, 2009.
- Benedetti, A., Morcrette, J., Boucher, O., Dethof, A., Engelen, R., Fisher, M., Flentje, H., Huneeus, N., Jones, L., and Kaiser, J.: Aerosol analysis and forecast in the European Centre for Medium-Range Weather Forecasts Integrated Forecast System: 2. Data assimilation, *J. Geophys. Res.*, 114, D13205, doi:10.1029/2008JD011115, 2009.
- Bishop, C. H., Etherton, B. J., and Majumdar, S. J.: Adaptive sampling with the ensemble transform Kalman filter. Part I: Theoretical aspects, *Mon. Weather Rev.*, 129, 420–436, 2001.
- Chen, D., Liu, Z., Fast, J., and Ban, J.: Simulations of Sulfate-Nitrate-Ammonium (SNA) aerosols during the extreme haze events over Northern China in October 2014, *Atmos. Chem. Phys. Discuss.*, doi:10.5194/acp-2016-222, in review, 2016.
- Chin, M., Rood, R. B., Lin, S. J., Muller, J. F., and Thompson, A. M.: Atmospheric sulfur cycle simulated in the global model GOCART: Model description and global properties, *J. Geophys. Res.-Atmos.*, 105, 24671–24687, 2000.
- Chin, M., Ginoux, P., Kinne, S., Torres, O., Holben, B.N., Duncan, B. N., Martin, R.V., Logan, J.A., Higurashi, A., and Nakajima, J.: Tropospheric aerosol optical thickness from the GOCART model and comparisons with satellite and Sun photometer measurements, *J. Atmos. Sci.*, 59(3), 461–483, 2002.
- Collins, W. D., Rasch, P. J., Eaton, B. E., Khattatov, B. V., and J.-F. Lamarque, J.-F.: Simulating aerosols using a chemical transport model with assimilation of satellite aerosol retrievals: Methodology for INDOEX, *J. Geophys. Res.*, 106, 7313–7336, 2001.
- de Meij, A., Krol, M., Dentener, F., Vignati, E., Cuvelier, C., and Thunis, P.: The sensitivity of

aerosol in Europe to two different emission inventories and temporal distribution of emissions, *Atmos. Chem. Phys.*, 6, 4287–4309, doi:10.5194/acp-6-4287-2006, 2006.

Dai, T., Schutgens, N.A.J., Goto, D. Shi, G.Y., Nakajima, T.: Improvement of aerosol optical properties modeling over Eastern Asia with MODIS AOD assimilation in a global non-hydrostatic icosahedral aerosol transport model, *Environ. Pollut.*, 195, 319–329, 2014.

Denby, B., Schaap, M., Segers, A.J., Builtjes, P.J.H., Horalek, J.: Comparison of two data assimilation methods for assessing PM10 exceedances on the European scale, *Atmos. Environ.*, 42 (30), 7122–7134, 2007.

Ding, J., van der A, R. J., Mijling, B., Levelt, P. F., and Hao, N.: NO<sub>x</sub> emission estimates during the 2014 Youth Olympic Games in Nanjing, *Atmos. Chem. Phys.*, 15, 9399–9412, doi:10.5194/acp-15-9399-2015, 2015.

Dubovik, O., Lapyonok, T., Kaufman, Y. J., Chin, M., Ginoux, P., Kahn, R. A., and Sinyuk, A.: Retrieving global aerosol sources from satellites using inverse modeling, *Atmos. Chem. Phys.*, 8, 209–250, doi:10.5194/acp-8-209-2008, 2008

Elbern, H., Strunk, A., Schmidt, H., and Talagrand, O.: Emission rate and chemical state estimation by 4-dimensional variational inversion, *Atmos. Chem. Phys.*, 7, 3749–3769, doi:10.5194/acp-7-3749-2007, 2007.

Evensen, G.: Sequential data assimilation with a nonlinear quasi-geostrophic model using Monte Carlo methods to forecast error statistics, *J. Geophys. Res.*, 99(C5), 10143–10162, 1994.

Freitas, S. R.; Longo, K. M.; Alonso, M. F.; Pirre, M.; Marecal, V.; Grell, G.; Stockler, R.; Mello, R. F.; Sánchez G ácita, M.. PREP-CHEM-SRC 1.0: a preprocessor of trace gas and aerosol emission fields for regional and global atmospheric chemistry models. *Geoscientific Model Development*, v. 4, p. 419–433, 2011.

Ginoux, P., Chin, M. Tegen, I., Prospero, J. M., Holben, B., Dubovik, O., and Lin, S.-J.: Sources and distributions of dust aerosols simulated with the GOCART model, *J. Geophys. Res.*, 106, 20,255–20,273, doi:10.1029/2000JD000053, 2001.

Grell, G., Peckham, S. E., Schmitz, R., McKeen, S. A., Frost, G., Skamarock, W. C., and Eder, B.: Fully coupled “online” chemistry within the WRF model, *Atmos. Environ.*, 39, 6957–6975, doi:10.1016/j.atmosenv.2005.04.027, 2005.

Guenther, A., Hewitt, C. N., Erickson, D., Fall, R., Geron, C., Graedel, T., Harley, P., Klinger, L.,

Lerdau, M., McKay, W., Pierce, T., Scholes, B., Steinbrecher, R., Tallamraju, R., Taylor, J.,  
 and Zimmerman, P.: A global model of natural volatile organic compound emissions, *J.*  
*Geophys. Res.*, 100, 8873–8892, doi:10.1029/94JD02950, 1995.

Guerrette, J. J. and Henze, D. K.: Development and application of the WRFPLUS-Chem online  
 chemistry adjoint and WRFDA-Chem assimilation system, *Geosci. Model Dev.*, 8,  
 1857-1876, doi:10.5194/gmd-8-1857-2015, 2015.

Hakami, A., Henze, D. K., Seinfeld, J. H., Chai, T., Tang, Y., Carmichael, G. R., and Sandu, A.:  
 Adjoint inverse modeling of black carbon during the Asian Pacific Regional Aerosol  
 Characterization Experiment, *J. Geophys. Res.-Atmos.*, 110, D14301,  
 doi:10.1029/2004JD005671, 2005.

Heemink, A.W., and Segers, A.J.: Modeling and prediction of environmental data in space and  
 time using Kalman filtering, *Stoch. Environ. Res. Risk Assess.* 16 (3), 225–240, 2002.

Henze, D. K., Hakami, A., and Seinfeld, J. H.: Development of the adjoint of GEOS-Chem,  
*Atmos. Chem. Phys.*, 7, 2413–2433, doi:10.5194/acp-7-2413-2007, 2007.

Henze, D. K., Seinfeld, J. H., and Shindell, D. T.: Inverse modeling and mapping US air quality  
 influences of inorganic PM<sub>2.5</sub> precursor emissions using the adjoint of GEOS-Chem, *Atmos.*  
*Chem. Phys.*, 9, 5877–5903, doi:10.5194/acp-9-5877-2009, 2009.

Houtekamer, P. L., Mitchell, H. L., Pellerin, G., Buehner, M., Charron, M., Spacek, L., and  
 Hansen, B.: Atmospheric data assimilation with an ensemble Kalman filter: Results with real  
 observations, *Mon. Weather Rev.*, 133, 604–620, 2005.

Ide, K., Courtier, P., Ghil, M., and Lorenc, A. C.: Unified notation for data assimilation:  
 operational, sequential and variational, *J. Meteorol. Soc. Japan*, 75, 181–189, 1997.

Jiang, Z., Liu, Z., Wang, T., Schwartz, C. S., Lin, H.-C., and Jiang, F.: Probing into the impact of  
 3DVAR assimilation of surface PM<sub>10</sub> observations over China using process analysis, *J.*  
*Geophys. Res. Atmos.*, 118, 6738–6749, doi:10.1002/jgrd.50495, 2013.

Peters, W., Jacobson, A. R., Sweeney, C., Andrews, A. E., Conway, T. J., Masarie, K., Miller, J.  
 B., Bruhwiler, L. M. P., Petron, G., Hirsch, A. I., Worthy, D. E. J., van der Werf, G.  
 R., Randerson, J. T., Wennberg, P. O., Krol, M. C., Tans, P. P.: An atmospheric perspective  
 on North American carbon dioxide exchange: CarbonTracker, *P. Natl. Acad. Sci. USA*, 104,  
 18925–18930, 2007.

Kahnert, M.: Variational data analysis of aerosol species in a regional CTM: Background error covariance constraint and aerosol optical observation operators, *Tellus, Ser. B*, 60, 753–770, doi:10.1111/j.1600-0889.2008.00377, 2008.

Kleist, D. T., Parrish, D. F., Derber, J. C., Treadon, R., Wu, W.-S., and Lord, S.: Introduction of the GSI into the NCEP global data assimilation system, *Weather Forecast.*, 24, 1691–1705, 2009.

Huneus, N., Chevallier, F., and Boucher, O.: Estimating aerosol emissions by assimilating observed aerosol optical depth in a global aerosol model, *Atmos. Chem. Phys.*, 12, 4585–4606, doi:10.5194/acp-12-4585-2012, 2012.

Huneus, N., Boucher, O., and Chevallier, F.: Atmospheric inversion of SO<sub>2</sub> and primary aerosol emissions for the year 2010, *Atmos. Chem. Phys.*, 13, 6555–6573, doi:10.5194/acp-13-6555-2013, 2013.

Hunt, B., Kostelich, E., and Szunyogh, I.: Efficient data assimilation for spatiotemporal chaos: a Local Ensemble Transform Kalman Filter, *Physica D*, 230, 112–126, 2007.

Lee, E.-H., Ha, J.-C., Lee, S.-S., and Chun, Y.: PM<sub>10</sub> data assimilation over South Korea to Asian dust forecasting model with the optimal interpolation method, *Asia-Pacific J. Atmos. Sci.*, 49(1), 73–85, doi:10.1007/s13143-013-0009-y, 2013.

Li, Z., Zang, Z., Li, Q. B., Chao, Y., Chen, D., Ye, Z., Liu, Y., and Liou, K. N.: A three-dimensional variational data assimilation system for multiple aerosol species with WRF/Chem and an application to PM<sub>2.5</sub> prediction, *Atmos. Chem. Phys.*, 13, 4265–4278, doi:10.5194/acp-13-4265-2013, 2013.

Li, J., Li, Y., Bo, Y., and Xie, S.: High-resolution historical emission inventories of crop residue burning in fields in China for the period 1990–2013, *Atmos. Environ.*, 138, 152–161, 2016.

Liu, Z., Liu, Q., Lin, H. C., Schwartz, C. S., Lee, Y. H., and Wang, T.: Three-dimensional variational assimilation of MODIS aerosol optical depth: implementation and application to a dust storm over East Asia, *J. Geophys. Res.*, 116, D23206, doi:10.1029/2011JD016159, 2011.

Liu, F., Zhang, Q., Tong, D., Zheng, B., Li, M., Huo, H., and He, K. B.: High-resolution inventory of technologies, activities, and emissions of coal-fired power plants in China from 1990 to 2010, *Atmos. Chem. Phys.*, 15, 13299–13317, doi:10.5194/acp-15-13299-2015, 2015.

McLinden, C.A., Fioletov, V., Shephard, M.W., Krotkov, N., Li, C., Martin, R.V., Moran, M.D., and J. Joiner,: Space-based detection of missing sulfur dioxide sources of global air pollution, *Nat. Geosci.*, 9, 496–500, doi:10.1038/ngeo2724, 2016.

Mijling, B. and van der A, R. J.: Using daily satellite observations to estimate emissions of short-lived air pollutants on a mesoscopic scale, *J. Geophys. Res.*, 117, D17302, doi:10.1029/2012JD017817, 2012.

Miyazaki, K., Eskes, H. J., Sudo, K., Takigawa, M., van Weele, M., and Boersma, K. F.: Simultaneous assimilation of satellite NO<sub>2</sub>, O<sub>3</sub>, CO, and HNO<sub>3</sub> data for the analysis of tropospheric chemical composition and emissions, *Atmos. Chem. Phys.*, 12, 9545– 9579, doi:10.5194/acp-12-9545-2012, 2012.

Miyazaki, K., Eskes, H. J., Sudo, K., and Zhang, C.: Global lightning NO<sub>x</sub> production estimated by an assimilation of multiple satellite data sets, *Atmos. Chem. Phys.*, 14, 3277–3305, doi:10.5194/acp-14-3277-2014, 2014.

Ott, E., Hunt, B. R., Szunyogh, I., Zimin, A. V., Kostelich, E. J., et al.: Exploiting local low dimensionality of the atmospheric dynamics for efficient Kalman filtering, *arXiv:physics/0203058*, 24 pp., available at: <http://arxiv.org/abs/physics/0203058v3/>, 2002.

Ott, E., Hunt, B. R., Szunyogh, I., Zimin, A. V., Kostelich, E. J., et al.: A local ensemble Kalman filter for atmospheric data assimilation, *Tellus A*, 56, 415–428, 2004.

Pagowski, M., Grell, G. A., McKeen, S. A., Peckham, S. E., and Devenyi, D.: Three-dimensional variational data assimilation of ozone and fine particulate matter observations: some results using the Weather Research and Forecasting – Chemistry model and Grid-point Statistical Interpolation, *Q. J. Roy. Meteor. Soc.*, 136, 2013–2024, doi:10.1002/qj.700, 2010.

Pagowski, M., and Grell, G. A.: Experiments with the assimilation of fine aerosols using an ensemble Kalman filter, *J. Geophys. Res.-Atmos.*, 117, D21302, doi:10.1029/2012jd018333, 2012.

Peng, Z., Zhang, M., Kou, X., Tian, X., and Ma, X.: A regional carbon data assimilation system and its preliminary evaluation in East Asia, *Atmos. Chem. Phys.*, 15, 1087–1104, doi:10.5194/acp-15-1087-2015, 2015.

Pope, C. A.: Review: Epidemiological basis for particulate air pollution health standards, *Aerosol Sci. Tech.*, 32, 4–14, 2000.

Pope, C. A., Burnett, R. T., Thun, M. J., Calle, E. E., Krewski, D., Ito, K., and Thurston, G. D.: Lung cancer, cardiopulmonary mortality, and long-term exposure to fine particulate air pollution, *J. Am. Med. Assoc.*, 287, 1132–1141, 2002.

Rubin, J. I., Reid, J. S., Hansen, J. A., Anderson, J. L., Collins, N., Hoar, T. J., Hogan, T., Lynch, P., McLay, J., Reynolds, C. A., Sessions, W. R., Westphal, D. L., and Zhang, J.: Development of the Ensemble Navy Aerosol Analysis Prediction System (ENAAPS) and its application of the Data Assimilation Research Testbed (DART) in support of aerosol forecasting, *Atmos. Chem. Phys.*, 16, 3927–3951, doi:10.5194/acp-16-3927-2016, 2016.

Saide, P. E., Carmichael, G. R., Liu, Z., Schwartz, C. S., Lin, H. C., da Silva, A. M., and Hyer, E.: Aerosol optical depth assimilation for a size-resolved sectional model: impacts of observationally constrained, multi-wavelength and fine mode retrievals on regional scale analyses and forecasts, *Atmos. Chem. Phys.*, 13, 10425–10444, doi:10.5194/acp-13-10425-2013, 2013.

Schwartz, C. S., Liu, Z., Lin, H. C., and McKeen, S. A.: Simultaneous three-dimensional variational assimilation of surface fine particulate matter and MODIS aerosol optical depth, *J. Geophys. Res.*, 117, D13202, doi:10.1029/2011JD017383, 2012.

Schwartz, C. S., Liu, Z., Lin, H.-C., and Cetola, J. D.: Assimilating aerosol observations with a “hybrid” variational-ensemble data assimilation system, *J. Geophys. Res. Atmos.*, 119, 4043–4069, doi:10.1002/2013JD020937, 2014.

Sekiyama, T. T., Tanaka, T. Y., Shimizu, A., and Miyoshi, T.: Data assimilation of CALIPSO aerosol observations, *Atmos. Chem. Phys.*, 10, 39–49, doi:10.5194/acp-10-39-2010, 2010.

Schutgens, N. A. J., Miyoshi, T., Takemura, T., and Nakajima, T.: Sensitivity tests for an ensemble Kalman filter for aerosol assimilation, *Atmos. Chem. Phys.*, 10, 6583–6600, doi:10.5194/acp-10-6583-2010, 2010.

Schutgens, N. A. J., Miyoshi, T., Takemura, T., and Nakajima, T.: Applying an ensemble Kalman filter to the assimilation of AERONET observations in a global aerosol transport model, *Atmos. Chem. Phys.*, 10, 2561–2576, doi:10.5194/acp-10-2561-2010, 2010.

Schutgens, N., Nakata, M., and Nakajima, T.: Estimating Aerosol Emissions by Assimilating Remote Sensing Observations into a Global Transport Model, *Remote Sensing*, 4, 3528–3543, 2012.



- Tang, X., Zhu, J., Wang, Z. F., and Gbaguidi, A.: Improvement of ozone forecast over Beijing based on ensemble Kalman filter with simultaneous adjustment of initial conditions and emissions, *Atmos. Chem. Phys.*, 11, 12901–12916, doi:10.5194/acp-11-12901-2011, 2011.
- Tombette, M., Mallet, V., and Sportisse, B.: PM10 data assimilation over Europe with the optimal interpolation method, *Atmos. Chem. Phys.*, 9, 57-70, doi:10.5194/acp-9-57-2009, 2009.
- Torn, R. D., Hakim, G. J., and Snyder, C.: Boundary conditions for limited-area ensemble Kalman filters, *Mon. Weather Rev.*, 134, 2490–2502, 2006.
- van Loon, M., Builtjes, P. J. H., and Segers, A. J.: Data assimilation of ozone in the atmospheric transport chemistry model LOTOS, *Environ. Model. Softw.*, 15, 603–609, 2000.
- Wang, J., Xu, X., Henze, D. K., Zeng, J., Ji, Q., Tsay, S.-C., and Huang, J.: Top-down estimate of dust emissions through integration of MODIS and MISR aerosol retrievals with the GEOS-Chem adjoint model, *Geophys. Res. Lett.*, 39, L08802, doi:10.1029/2012GL051136, 2012.
- Wang, Y. X., Zhang, Q. Q., Jiang, J. K., Zhou, W., Wang, B. Y., He, K. B., Duan, F. K., Zhang, Q., Philip, S., and Xie, Y. Y.: Enhanced sulfate formation during China's severe winter haze episode in January 2013 missing from current models, *J. Geophys. Res.-Atmos.*, 119, 10.1002/2013JD021426, 2014
- Wang, X.Y., Liang, X.Z., Jiang, W.M., Tao, Z.N., Wang, J.X.L., Liu, H.N., Han Z.W., Liu, S.Y., Zhang, Y.Y., Grell, G.A., Peckham, S.E.: WRF-Chem simulation of East Asian air quality: Sensitivity to temporal and vertical emissions distributions, *Atmospheric Environment*, 44(2010) 660-669
- Whitaker, J. S., and Hamill, T. M.: Ensemble data assimilation without perturbed observations, *Mon. Weather Rev.*, 130, 1913–1924, 2002.
- Woo, J.H., Baek, J.M., Kim, J.W., Carmichael, G.R., Thongboonchoo, N., Kim, S.T., An, J.H.: Development of a Multi-Resolution Emission Inventory and Its Impact on Sulfur Distribution for Northeast Asia, *Water, Air, and Soil Pollution* 148: 259–278, 2003.
- Weekly Crop Residue Burning Monitoring Report ,  
<http://hjj.mep.gov.cn/jgis/201510/P020151012746205487305.pdf>, 2015a (in Chinese).
- Weekly Crop Residue Burning Monitoring Report,

<http://hjj.mep.gov.cn/jgjs/201510/P020151019568921489639.pdf>, 2015b(in Chinese).

Xia Y., Zhao, Y., Nielsen, C.P., Benefits of China's efforts in gaseous pollutant control indicated by the bottom-up emissions and satellite observations 2000-2014, *Atmospheric Environment*, 136, 43-53, 2016

Yu, H., Dickinson, R. E., Chin, M., Kaufman, Y. J., Geogdzhayev, B., and Mishchenko, M. I.: Annual cycle of global distributions of aerosol optical depth from integration of MODIS retrievals and GOCART model simulations, *J. Geophys. Res.*, 108(D3), 4128, doi:10.1029/2002JD002717, 2003.

Yumimoto, K., Uno, I., Sugimoto, N., Shimizu, A., and Satake, S.: Adjoint inverse modeling of dust emission and transport over East Asia, *Geophys. Res. Lett.*, 34, L00806, doi:10.029/2006GL028551, 2007.

Yumimoto, K., Uno, I., Sugimoto, N., Shimizu, A., Liu, Z., and Winker, D. M.: Adjoint inversion modeling of Asian dust emission using lidar observations, *Atmos. Chem. Phys.*, 8, 2869-2884, doi:10.5194/acp-8-2869-2008, 2008.

Yumimoto, K., Nagao, T.M., Kikuchi, M., Sekiyama, T.T, Murakami, H., Tanaka, T.Y., Ogi, A., Irie, H., Khatri, P., Okumura, H., Arai, K., Morino, I., Uchino, O., Maki, T.: Aerosol data assimilation using data from Himawari-8, a next-generation geostationary meteorological satellite, *Geophys. Res. Lett.*, 43, 5886–5894, 2016.

Yin, X.M., Dai, T., Xin, J.Y., Gong, D.Y., Yang, J., Teruyuki, N., Shi, G.Y.: Estimation of aerosol properties over the Chinese desert region with MODIS AOD assimilation in a global model, *Adv. Clim. Change Res.*, 7, 90–98, 2016.

Zhang, J., Reid, J. S., Westphal, D., Baker, N., and Hyer, E.: A System for Operational Aerosol Optical Depth Data Assimilation over Global Oceans, *J. Geophys. Res.*, 113, D10208, doi:10.1029/2007JD009065, 2008.

Zhang, Q., Streets, D. G., Carmichael, G. R., He, K. B., Huo, H., Kannari, A., Klimont, Z., Park, I. S., Reddy, S., Fu, J. S., Chen, D., Duan, L., Lei, Y., Wang, L. T., and Yao, Z. L.: Asian emissions in 2006 for the NASA INTEX-B mission, *Atmos. Chem. Phys.*, 9, 5131-5153, doi:10.5194/acp-9-5131-2009, 2009.

Zhang, L., Liu, L. C., Zhao, Y. H., Gong, S. L., Zhang, X. Y., Henze, D. K., Capps, S. L., Fu, T. M., Zhang, Q., and Wang, Y. X.: Source attribution of particulate matter pollution over

968 North China with the adjoint method, *Environ.Res.Lett.*, 10, Artn  
969 08401110.1088/1748-9326/10/8/084011, 2015.

970 Zheng, B., Zhang, Q., Zhang, Y., He, K. B., Wang, K., Zheng, G. J., Duan,  
971 F. K., Ma, Y. L., and Kimoto, T.: Heterogeneous chemistry: a mechanism  
972 missing in current models to explain secondary inorganic aerosol formation  
973 during the January 2013 haze episode in North China, *Atmos.Chem.Phys.*, 15, 2031-2049,  
974 10.5194/acp-15-2031-2015, 2015.

975

976

## List of Figures and Table

Figure 1. Locations of 77 PM<sub>2.5</sub> assimilation observation stations (black dot) and the 77 independent observation stations (red triangle) in the model domain. The three colored boxes mark sub-regions with relatively dense coverage for the Beijing–Tianjin–Hebei region (JJJ, 12 assimilation stations and 12 independent stations, red box), the Yangtze River delta (YRD, 24 assimilation stations and 24 independent stations, blue box) and the Pearl River delta (PRD, 9 stations and 9 independent stations, green box).

Figure 2. (a) Framework of  $M_{SF}$  and (b) flow chart of the data assimilation system that simultaneously optimizes the chemical initial conditions and emissions.

Figure 3. Time series of prior ensemble mean RMSE and total spread for PM<sub>2.5</sub> concentrations aggregated over all observations over the three sub-regions: (a) Beijing–Tianjin–Hebei region; (b) Yangtze River delta; (c) Pearl River delta; and (d) time series of the area mean ensemble spread for  $\lambda_{PM2.5}$  over the three sub-regions.

Table 1. Comparison of the surface PM<sub>2.5</sub> mass concentrations from the control and assimilation experiments to observations over all analysis times from 6 to 16 October 2014.

Figure 4. Spatial distribution of the PM<sub>2.5</sub> mass ( $\mu\text{g}\cdot\text{m}^{-3}$ ) of the (a) observations; (b) simulation of the control run; (c) analysis of expJ; (d) analysis of expC; (e) increments of expJ; (f) increments of expC; at the lowest model level averaged over all hours from 6 to 16 October 2014.

Figure 5. Hourly area-averaged time series of emission scaling factors (black) extracted from the ensemble mean of the analyzed  $\lambda_{PM2.5}^a$  and the corresponding analyzed unspeciated primary PM<sub>2.5</sub> emissions  $E_{PM2.5}^a$  (blue) over the three sub-regions: (a) Beijing–Tianjin–Hebei region; (b) Yangtze River delta; and (c) Pearl River delta.

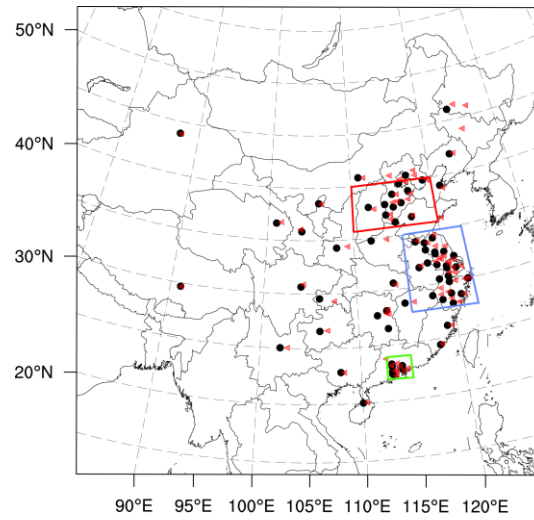
Figure 6. Spatial distribution of  $\lambda_{PM2.5}$  at the lowest model level averaged over all hours from 6 to 16 October 2014.

Figure 7. Spatial distribution of (a) the prior unspeciated primary sources of PM<sub>2.5</sub> ( $\mu\text{g}\cdot\text{m}^{-2}\text{ s}^{-1}$ ) and (b) the time-averaged differences between the ensemble mean analysis and the prior values ( $\mu\text{g}\cdot\text{m}^{-2}\text{ s}^{-1}$ ) at the lowest model level averaged over all hours from 6 to 16 October 2014.

Figure 8. Time series of the hourly PM<sub>2.5</sub> obtained from observations (circle), analysis (blue line), control run (black line) and hourly output of 48-h forecast in three megacities: (a) Beijing; (c) Shanghai; and (e) Guangzhou in expJ and (b) Beijing; (d) Shanghai; and (f) Guangzhou in expC. See text in section 5.4.

Figure 9. Bias of surface PM<sub>2.5</sub> as a function of forecast range calculated against independent observations over the three sub-regions: (a) Beijing–Tianjin–Hebei region; (c) Yangtze River delta; (e) Pearl River delta and RMSE over (b) Beijing–Tianjin–Hebei region; (d) Yangtze River delta; (f) Pearl River delta; (g) Normalized RMSE (assimilation divided by control) for expJ and (h) (g) Normalized RMSE for expC.

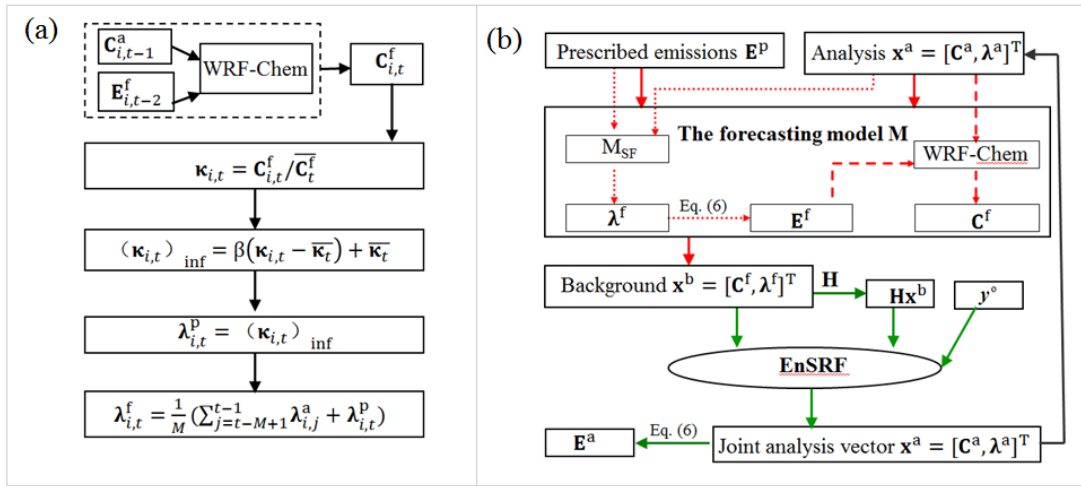
1028  
1029  
1030



1031

1032 Figure 1. Locations of 77  $\text{PM}_{2.5}$  assimilation observation stations (black dot) and the  
1033 77 independent observation stations (red triangle) in the model domain. The three  
1034 colored boxes mark sub-regions with relatively dense coverage for the Beijing–  
1035 Tianjin–Hebei region (JJJ, 12 assimilation stations and 12 independent stations, red  
1036 box), the Yangtze River delta (YRD, 24 assimilation stations and 24 independent  
1037 stations, blue box) and the Pearl River delta (PRD, 9 stations and 9 independent  
1038 stations, green box).  
1039

1040



1041

1042

1043

1044

Figure 2. (a) Framework of  $M_{SF}$  and (b) flow chart of the data assimilation system that simultaneously optimizes the chemical initial conditions and emissions.

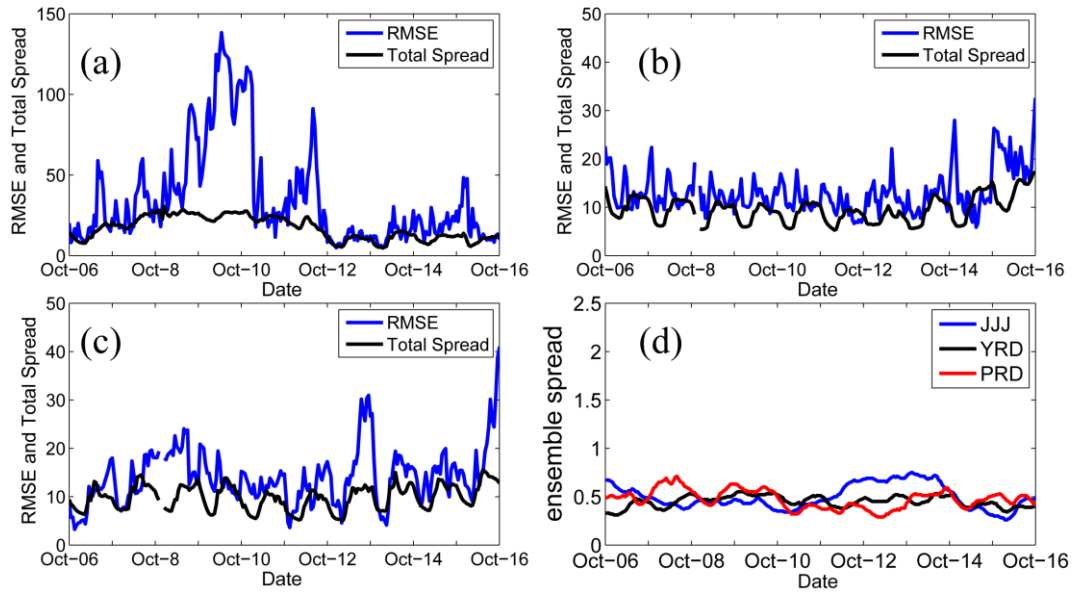


Figure 3. Time series of prior ensemble mean RMSE and total spread for  $\text{PM}_{2.5}$  concentrations aggregated over all observations over the three sub-regions: (a) Beijing–Tianjin–Hebei region; (b) Yangtze River delta; (c) Pearl River delta; and (d) time series of the area mean ensemble spread for  $\lambda_{\text{PM}_{2.5}}$  over the three sub-regions.



Table 1. Comparison of the surface PM<sub>2.5</sub> mass concentrations from the control and assimilation experiments to observations over all analysis times from 6 to 16 October 2014.

Region	Experiment	Mean observed	Mean simulated	BIAS	RMSE	CORR
		value	value			
Beijing–	Control		98.3	−18.0	81.6	0.790
Tianjin–	expJ	116.3	106.0	−10.3	66.9	0.827
Hebei	expC		104.1	−12.2	64.0	0.845
Yangtze	Control		64.4	15.9	30.6	0.593
River	expJ	48.5	46.9	−1.6	15.3	0.846
delta	expC		46.1	−2.4	17.3	0.803
Pearl	Control		82.4	20.6	31.8	0.624
River	expJ	61.8	66.5	4.7	16.1	0.800
delta	expC		64.1	−2.3	15.6	0.797

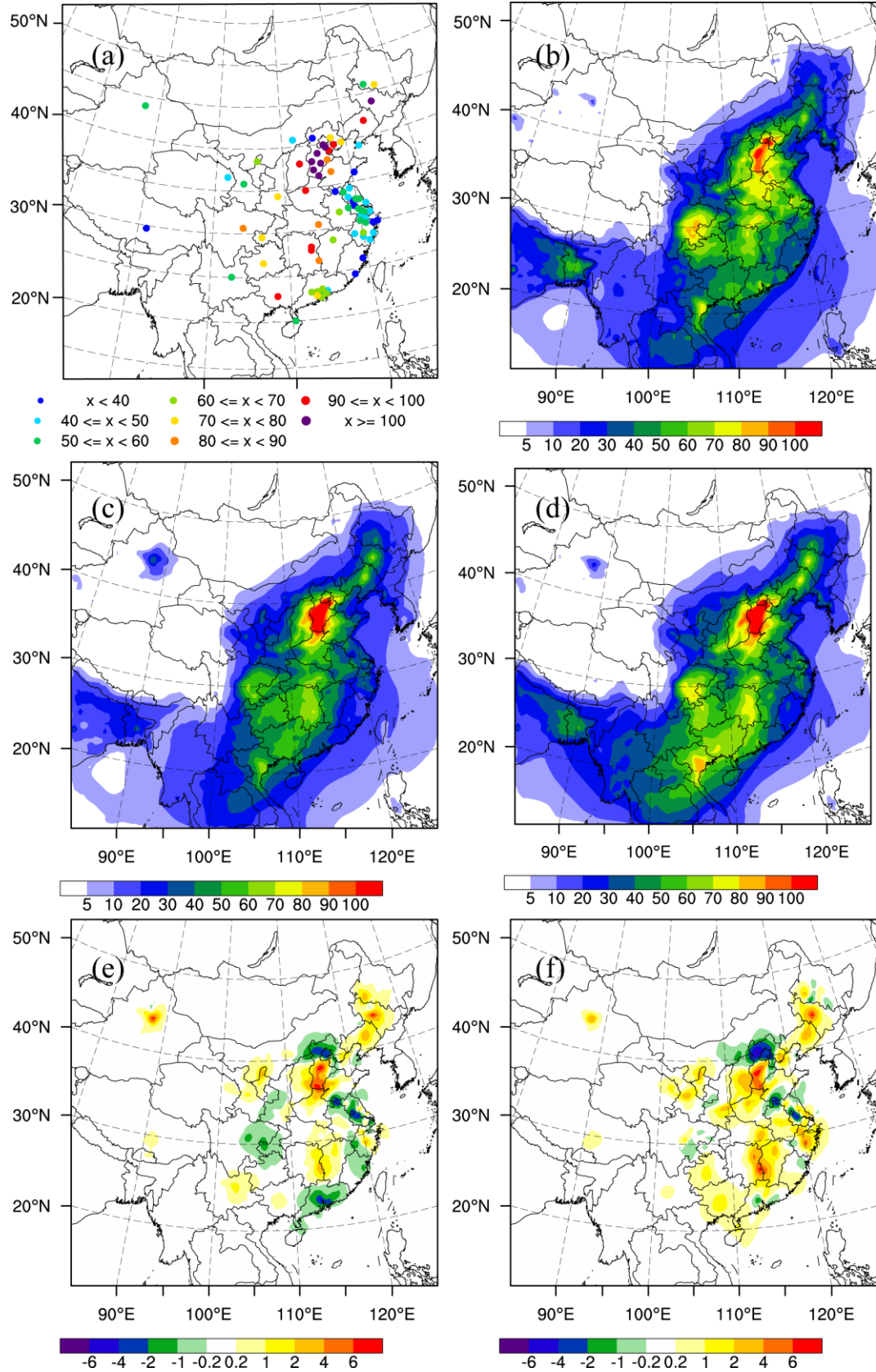
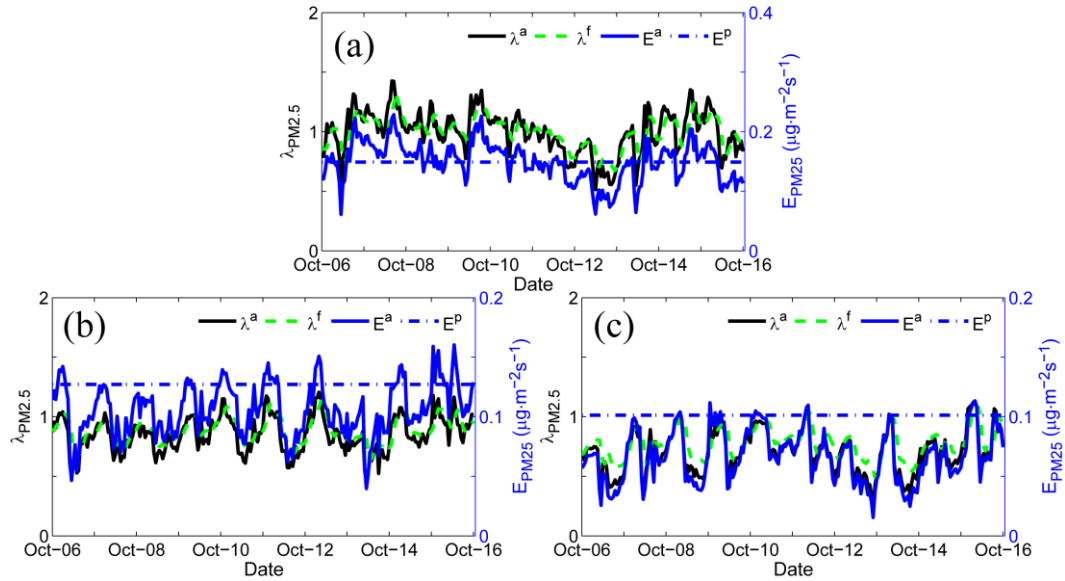


Figure 4. Spatial distribution of the PM<sub>2.5</sub> mass ( $\mu\text{g m}^{-3}$ ) of the (a) observations; (b) simulation of the control run; (c) analysis of expJ; (d) analysis of expC; (e) increments of expJ; (f) increments of expC; at the lowest model level averaged over all hours



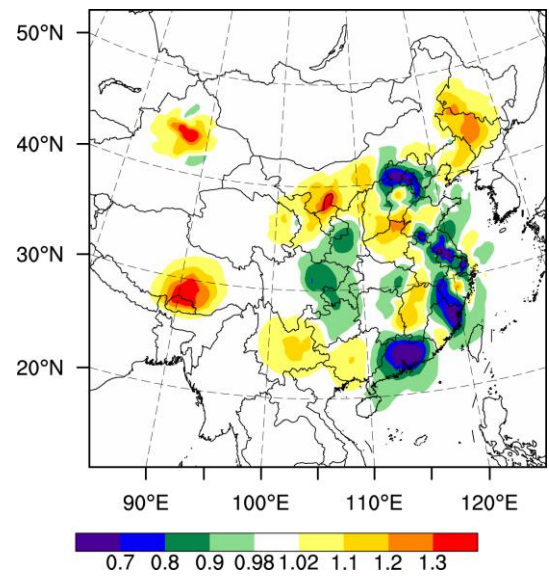
1064  
1065  
1066



1067  
1068  
1069  
1070  
1071  
1072  
1073

Figure 5. Hourly area-averaged time series of emission scaling factors (black) extracted from the ensemble mean of the analyzed  $\lambda_{\text{PM}_{2.5}}^a$  and the corresponding analyzed unspiciated primary  $\text{PM}_{2.5}$  emissions  $E_{\text{PM}_{2.5}}^a$  (blue) over the three sub-regions: (a) Beijing–Tianjin–Hebei region; (b) Yangtze River delta; and (c) Pearl River delta.

1074



1075

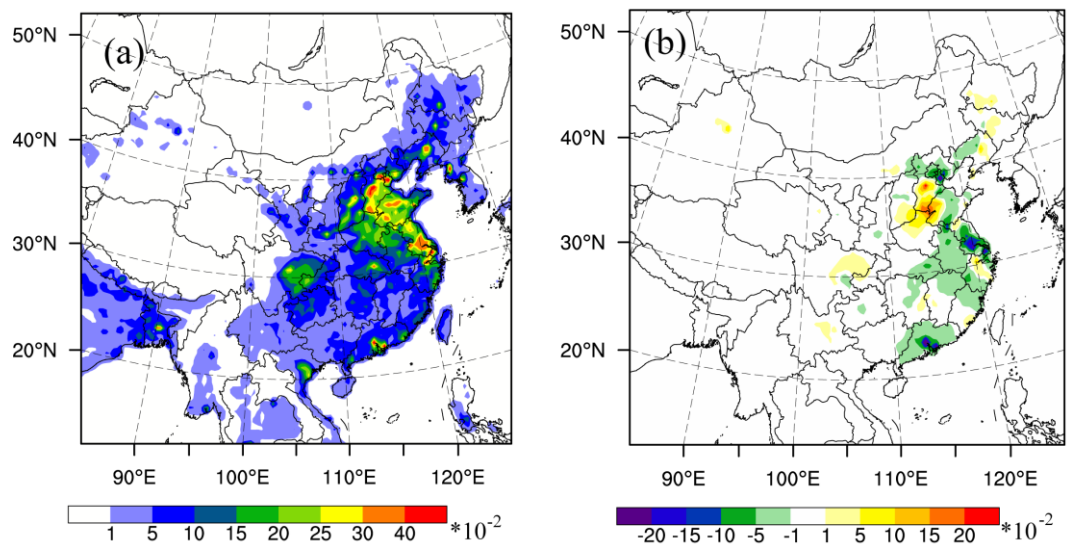
1076

1077

1078

Figure 6. Spatial distribution of  $\lambda_{PM2.5}$  at the lowest model level averaged over all hours from 6 to 16 October 2014.

1079

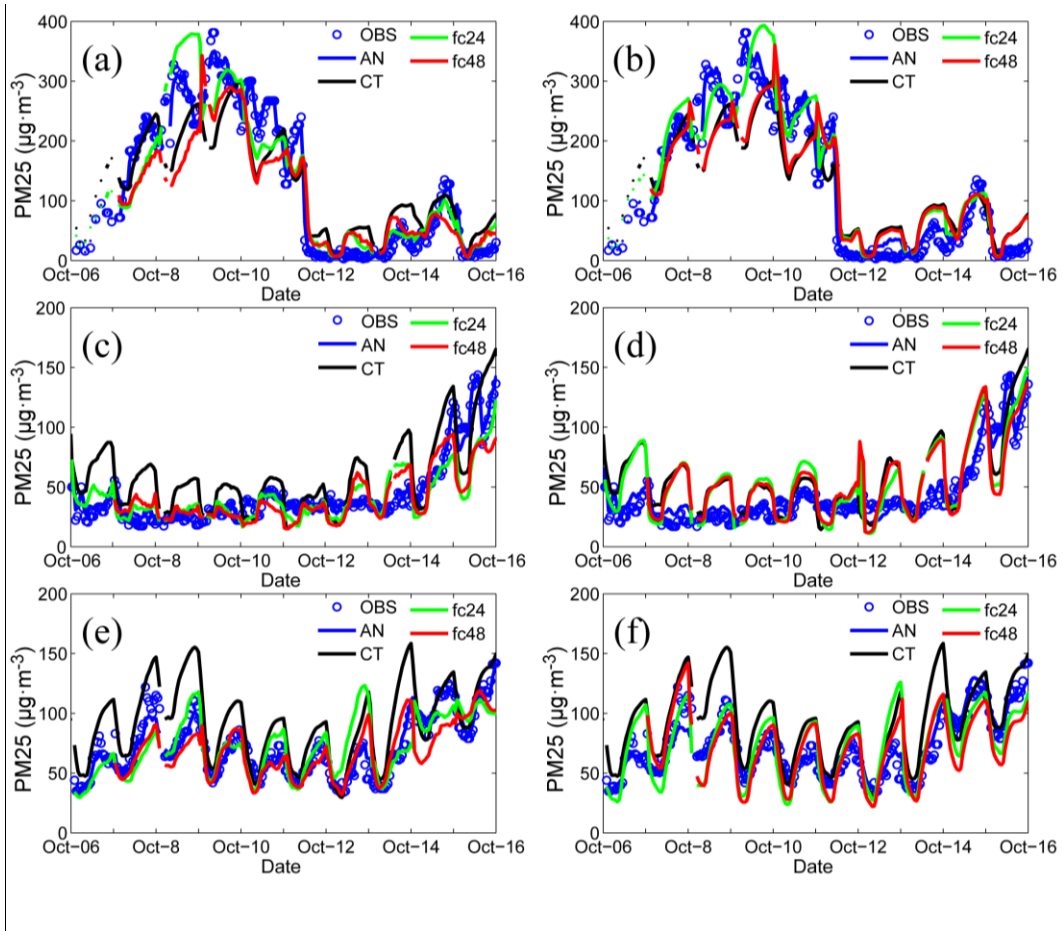


1080

1081 Figure 7. Spatial distribution of (a) the prior unspeciated primary sources of PM<sub>2.5</sub>  
1082 ( $\mu\text{g m}^{-2} \text{s}^{-1}$ ) and (b) the time-averaged differences between the ensemble mean  
1083 analysis and the prior values ( $\mu\text{g m}^{-2} \text{s}^{-1}$ ) at the lowest model level averaged over all  
1084 hours from 6 to 16 October 2014.

1085

1086



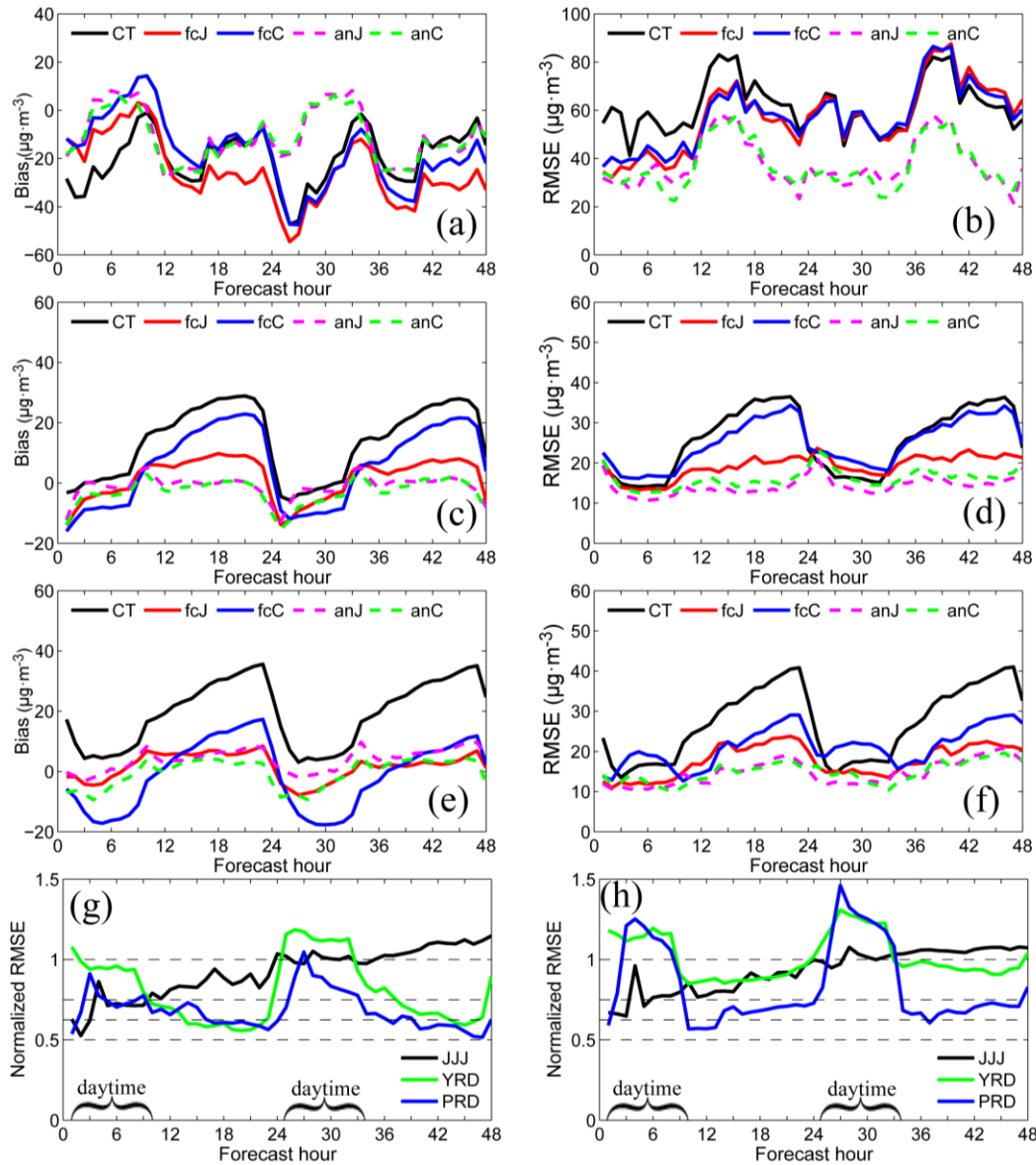
1088

1089 Figure 8. Time series of the hourly  $PM_{2.5}$  obtained from observations (circle), analysis  
 1090 (blue line), control run (black line) and hourly output of 48-h forecast in three  
 1091 megacities: (a) Beijing; (c) Shanghai; and (e) Guangzhou in expJ and (b) Beijing; (d)  
 1092 Shanghai; and (f) Guangzhou in expC. See text in section 5.4.

1093

1094

1095



1096

1097

1098

1099

1100

1101

1102

Figure 9. Bias of surface  $\text{PM}_{2.5}$  as a function of forecast range calculated against independent observations over the three sub-regions: (a) Beijing-Tianjin-Hebei region; (c) Yangtze River delta; (e) Pearl River delta and RMSE over (b) Beijing-Tianjin-Hebei region; (d) Yangtze River delta; (f) Pearl River delta; (g) Normalized RMSE (assimilation divided by control) for expJ and (h) (g) Normalized RMSE for expC.